Accepted Manuscript

Field and laboratory validation of remote rover operations Science Team findings: The CanMars Mars Sample Return analogue mission

Christy M. Caudill, Gordon R. Osinski, Eric Pilles, Haley M. Sapers, Alexandra J. Pontefract, Raymond Francis, Shamus Duff, Joshua Laughton, Jonathan O'Callaghan, Racel Sopoco, Gavin Tolometti, Michael Tuite, Kenneth H. Williford, Tianqi Xie

PII: S0032-0633(18)30065-5

DOI: https://doi.org/10.1016/j.pss.2019.06.006

Reference: PSS 4682

To appear in: *Planetary and Space Science*

Received Date: 16 February 2018

Revised Date: 24 April 2019

Accepted Date: 14 June 2019

Please cite this article as: Caudill, C.M., Osinski, G.R., Pilles, E., Sapers, H.M., Pontefract, A.J., Francis, R., Duff, S., Laughton, J., O'Callaghan, J., Sopoco, R., Tolometti, G., Tuite, M., Williford, K.H., Xie, T., Field and laboratory validation of remote rover operations Science Team findings: The CanMars Mars Sample Return analogue mission, *Planetary and Space Science* (2019), doi: https://doi.org/10.1016/j.pss.2019.06.006.

Field and laboratory validation of remote rover operations Science Team findings: The CanMars Mars Sample Return Analogue Mission

Christy M. Caudill[1], Gordon R. Osinski [1,2], Eric Pilles[1], Haley M. Sapers[3], Alexandra J. Pontefract[4], Raymond Francis, Shamus Duff[1], Joshua Laughton[1], Jonathan O'Callaghan[1], Racel Sopoco[1], Gavin Tolometti[1], Michael Tuite[5], Kenneth H. Williford[5], Tianqi Xie[1]

[1] Centre for Planetary Science and Exploration / Dept. Earth Sciences, University of Western Ontario, 1151 Richmond St, London, ON, N6A 3K7 Canada
[2] Dept. Physics and Astronomy, University of Western Ontario, 1151 Richmond St, London, ON, N6A 3K7 Canada
[3] Jet Propulsion Laboratory, California Institute of Technology, Pasadena, California, USA; California Institute of Technology, Pasadena, California, USA; Dept. of Earth Sciences, University of Southern California, USA
[4] Department of Earth, Atmospheric and Planetary Science, Massachusetts Institute of Technology, Cambridge MA 02139 USA
[5] Jet Propulsion Laboratory, California Institute of Technology, Pasadena, CA 91109 USA

Corresponding author: C. M. Caudill, ccaudill@uwo.ca, ph. +1 520-488-6859

Abstract

The CanMars Mars Sample Return Analogue Deployment (MSRAD) was a closely simulated end-to-end Mars Sample Return (MSR) mission scenario, with instrumentation, goals, and constraints modeled on the upcoming NASA Mars 2020 rover mission. The exercise utilized the CSA Mars Exploration Science Rover (MESR) rover, deployed to Utah, USA, at a Mars-analogue field site. The principal features of the field site located near Green River, Utah, are Late Jurassic inverted, fluvial paleochannels, analogous to features on Mars in sites being considered for the ESA ExoMars rover mission and present within the chosen landing site for the Mars 2020 rover mission. The in-simulation ("in-sim") mission operations team worked remotely from The University of Western Ontario, Canada. A suite of MESR-integrated and hand-held spectrometers was selected to mimic those of the Mars 2020 payload, and a Utah-based, on-site team was tasked with field operations to carry out the data collection as commanded by the in-sim team. The field team also acquired the samples as chosen by the in-sim mission control team. As a validation of the in-sim mission science findings, the field team performed an independent geological assessment. This paper documents the field team's on-site geological assessment and subsequent laboratory and analytical results, then offers a comparison of mission (in-sim) and post-mission (laboratory) science results. The laboratory-based findings were largely consistent with the in-sim rover-derived data and geological interpretations, though some notable exceptions highlight the inherent difficulties in remote science. In some cases, available data was insufficient for lithologic identification given the absence of other important contextual information (e.g., textural information). This study suggests that the in-sim instruments were adequate for the Science Team to characterize samples; however, rover-based field work is necessarily hampered by mobility and time constraints with an obvious effect on efficiency but also precision, and to some extent, accuracy of the findings. Our data show a dearth of preserved total organic carbon (TOC) – used as a proxy for ancient biosignature preservation potential – in the fluvial-lacustrine system of this field site, suggesting serious consideration with respect to the capabilities and opportunities for addressing the Mars exploration goals. We therefore suggest a thorough characterization of terrestrial sites analogous to those of Mars rover landing sites, and in-depth field studies like CanMars as important, pre-mission strategic exercises.

Keywords: Mars, rover, analogue mission, sample return, mission operations

1. Introduction

The return of samples from Mars is a high priority of the international science community (e.g., NAS, 2013). The CanMars analogue mission was a multi-year, multi-national effort to undertake the most realistic simulation of remote rover operations for a Mars Sample Return (MSR) mission scenario to date (Osinski et al., 2019). The goals of the analogue mission were to understand and refine the strategic and tactical science and engineering operations procedures of a remote rover mission, based on the mission goals, requirements, and constraints of the upcoming NASA Mars 2020 rover mission. The science objectives and priorities for an MSR mission have been defined by the MSR End-to-End International Science Analysis Group (E2E-iSAG) as the Mars Exploration Planning and Analysis Goals (MEPAG; McLennan et al., 2012). The highest priority objective defined by the E2E-iSAG group is to "critically assess any evidence for past life or its chemical precursors, and place detailed constraints on the past habitability and the potential for preservation of the signs of life". A primary outcome of the CanMars analogue mission was the development of specific protocols and analytical approaches geared at achieving the three highest priority MSR science sub-objectives identified by MEPAG; namely: 1) Identify environments that were habitable in the past, and characterize conditions and processes that may have influenced the degree or nature of habitability therein; 2) Assess the potential of conditions and processes to have influenced preservation or degradation of biosignatures and evidence of habitability, from the time of formation to the time of observation. Identify specific deposits and subsequent geological conditions that have high potential to have preserved individual or multiple types of biosignatures; and 3) Determine if biosignatures of a prior ecosystem are present.

The 5-week CanMars analogue mission (beginning in 2015 and continuing in 2016) utilized the Canadian Space Agency (CSA) Mars Exploration Science Rover (MESR) rover hardware and software, built by MDA Maxar, and included an array of spectrometers and imagers to mimic those aboard Mars 2020 (Fig. 1). The CanMars instrument suite and the Mars 2020 equivalent instruments are detailed by (Osinski et al., 2019). Briefly, 785 nm Delta Nu Rockhound Raman and 532 B&W Tek i-Raman spectrometers were used as a stand-in for the Scanning Habitable Environments with Raman & Luminescence for Organics & Chemicals (SHERLOC; Beegle et al., 2015), capable of detecting potential organic and mineralogical biomarkers in situ. An Analytical Spectral Devices (ASD) TerraSpec handheld point spectrometer was used as a stand-in for the Mars 2020 SuperCam (Wiens et al., 2017) visible and infrared (VIS-IR), collecting data over 0.35–1.0 µm (visible-near infrared; VNIR) and 1.0–2.5 µm (short-waved infrared; SWIR) ranges. Both Raman and NIR spectroscopy can be used to identify organic functional groups and determine mineralogy (e.g., Table 1), so they produce highly synergistic data sets (Speight, 2017; Eshelman et al., 2014; Izawa et al., 2014). The SuperCam suite furthermore uses Laser Induced Breakdown Spectroscopy (LIBS) to study the geochemistry of rocks and soils, which was simulated using a field-portable SciAps portable LIBS with a 500 µm beam diameter, acquiring quantitative in situ elemental compositions with sensitivities ranging from 10 ppm for Li to 500–22,000 ppm for other elements. The Mars 2020 Planetary Instrument for X-ray Lithochemistry (PIXL) micro-focus X-ray fluorescence (XRF) spectrometer measures elemental chemistry at sub-millimeter scales, as does the CanMars stand-in Bruker Tracer IV-SD energy dispersive XRF field spectrometer. Finally, the Remote Micro-Imager (RMI) capability of SuperCam was achieved using a digital single-lens reflex (DSLR) camera. Figure 1 provides a comparison of Mars 2020 rover instruments, the CanMars instrument equivalents, and the post-mission validation laboratory instrumentation and data types.

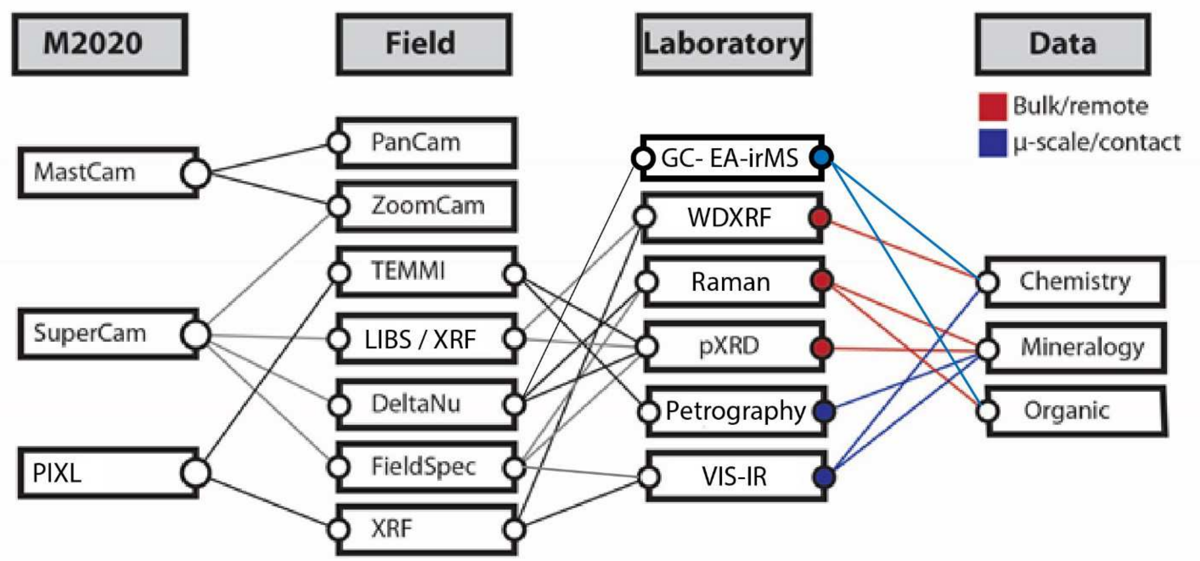

Figure 1. Schematic diagram showing the correlation between Mars 2020 (M2020) instruments, the CanMars M2020 stand-in field instruments (Field), and post-mission laboratory analyses used throughout this study. For definitions of laboratory collection methods, see Table 1. The far-right column indicates the type of laboratory data and scale appropriate to confirm in situ, in-sim science.

Table 1. Laboratory analytical techniques used in this study for both in-sim and out-of-sim samples.

Technique	Justification	Significance
Wavelength Dispersive X-ray Fluorescence spectrometry (WD-XRF)	Establish the presence and concentration of biologically relevant elements. Validate findings from in-sim XRF and LIBS data collection.	If colonized, microbial metabolism will alter the relationship between biologically relevant elements in the substrate and media

Raman spectroscopy	Determine mineralogy and physiochemical conditions based on the available spectral range. Validate findings from in-sim Raman data collection.	Non-destructive technique to produce a spectrum from a combination of molecular vibrations that is characteristic of organic as well as inorganic materials.
Powder X-ray Diffraction (pXRD)	Determine mineralogy, specifically the presence of crystalline, poorly crystalline, and amorphous phases based on peak shape. Validate mineralogic interpretations from in-sim data.	Bioavailability of elements varies depending on the geological substrate with amorphous mineral phases being the most bioavailable.
Optical microscopy	Determine the relationship between phases established by XRD; validate XRD; establish porosity and permeability for each phase. Validate findings from in-sim TEMMI data collection.	Crystallinity and mineral assemblages affect bioavailability of elements,
Visible-Infrared spectroscopy (VIS-IR)	Determine mineralogy and physiochemical conditions based on the available spectral range. Validate findings from in-sim VIS-IR data collection.	Spectral range producing absorptions from molecular vibrations that are characteristic of ferric and ferrous iron-bearing minerals, clays, carbonates, and sulfates.
Elemental Analyzer Isotope Ratio Mass Spectrometry (EA-irMS)	Analysis of total organic carbon (TOC) and $d^{13}C$.	Aromatics and aliphatic organics (e.g., kerogen) in the form of organic carbon are signs of ancient life preserved in sedimentary rocks that have been degraded by bacterial and chemical processes.
Solvent extraction Gas Chromatography Mass Spectrometry (GC-MS)	Analysis of molecular composition.	Analytical method developed for the analysis of organic acids in biological samples, allowing for their identification.

In addition to this instrumentation, three camera systems were integrated into MESR to simulate PanCam (Coates et al., 2017), with high-resolution cameras capable of panoramas and zoom images, as well a "belly cam" similar to the MSL HazCam system. Additional MESR-integrated instruments used in the CanMars mission included a LiDAR, mini-corer, and the three-dimensional exploration multispectral, microscopic imager (TEMMI; Bourassa et al., 2019). As most of the science instruments were hand-held and not MESR-integrated at the time of deployment, an on-site team was tasked with field operations to carry out the *in situ* data collection "commands"; the field team then uplinked the instrument data that was requested for each sol (each mission day) as if the data had been collected by the rover.

An overview of the in-sim application of the MESR-integrated and stand-in instruments during daily, or Tactical, planning in the CanMars mission and the use of this data by the Science Team is described by Caudill et al. (2019). Instrument data collection methods of the field team are described in this paper as an out-of-simulation, or "out-of-sim", activity. Where appropriate, specific recommendations will be offered in support of future analogue missions or activities with similar objectives to CanMars.

A major benefit, and motivation, for conducting analogue missions is the ability to compare rover mission-derived results to those of traditional geological field techniques and laboratory instrument-derived data. This paper details the post-CanMars traditional geological fieldwork of the CanMars site near Green River, Utah including mapping and sampling and the results of laboratory sample analysis. The total sample suite includes the "drilled, cached, MSR" samples selected by the Science Team, as described in Caudill et al. (2019) and an "out-of-sim" field sample suite collected by the field team to validate the in-sim findings and determine larger geological context.

2. Geological setting of the field site

The fidelity of the CanMars analogue mission required that the in-sim Mission Control Team not know the location of the landing site; thus, the team did not have access to previous geologic studies of the area. Indeed, this work represents the first published in-depth geologic characterization and laboratory analyses on the site.

The field site is located at ~1,300 m above sea level in a desert climate on the Colorado Plateau. The geology of this region locally consists of a variety of clastic and chemical sedimentary rocks. The clastic rocks include conglomerates, sandstones, shales, and mudstones ranging from Jurassic to Cretaceous in age (Hintze and Kowallis, 2009), with the Late-Jurassic Brushy Basin Member of the Morrison Formation being present in the CanMars field area. The principle landforms consist of inverted paleochannels, formed when strongly-cemented or otherwise strongly-indurated channel-fill deposits act as a capping unit, protecting less indurated or consolidated material from differential erosion (Williams et al., 2011). In the CanMars field area, a conglomeratic unit capped very fine-grained sedimentary rock, and the highly erosional regime that followed their deposition left behind sinuous, positive relief features.

Paleochannel formations throughout region have been mapped as non-continuous, low-sinuosity channel segments that vary in scale and morphology as well as depositional setting (including different source material and geochemistry of diagenetic waters). Derr (1974) mapped three channel segments in the same general area as this study, west of Green River, as the Late Jurassic-aged Brushy Basin Member of the Morrison Formation. These predominately mudstone channels are capped by fluvially-emplaced conglomerates that show multiple flow directions. The Morrison Formation also features a diverse assemblage of fossil vertebrates including a high abundance of microvertebrates (Foster, 2003). Spanning Utah, Colorado, Wyoming, Montana, New Mexico, and Northern Arizona, much of the work on the Morrison Formation has focused on dinosaur discoveries particularly in Colorado. The geology of the inverted paleochannel features that dominate the CanMars field site in Utah, however, are comparatively understudied. Derr (1974) and Williams et al. (2011) documented the lithology of the Brushy Basin Member as discontinuous fine to medium-grained sandstones overlain by red, purple, gray, and green mudstones having a popcorn-like weathered surface texture, emplaced from extensive floodplains with lake deposits in a semi-arid environment. Discontinuous patches of deep lacustrine limestone have also been observed (Craig et al., 1955; Williams et al., 2011). The popcorn texture is indicative of tuffaceous mudstones, comprised of secondary clays from aqueously-altered silicic volcanic ash that was emplaced in the lakes during volcanic eruptions west and southwest of the field site (Demko et al., 2004). These altered ash deposits provide an excellent analogue for the investigation of clay-rich, ancient terrains of Mars (e.g., McKeown et al., 2011).

The inverted paleochannel features and their emplacement in a semi-arid environment which transitioned to an arid, erosional regime are important for studies of ancient terrains on Mars. The ancient terrains of Mars have preserved sedimentary deposits that record fluvial activity, including channels, lakes (e.g., Gale Crater; Grotzinger et al., 2015), and even tens of km-scale deltaic deposits (e.g., Ebserswalde Crater; Rice et al., 2013 and Jezero Crater; Fassett and Head, 2005). Inverted channel deposits in these regions on Mars are relatively common (e.g., Malin and Edgett, 2003), and present an opportunity to explore exposures of soft sedimentary material that has been protected from erosion by a capping unit. Fluvial-lacustrine sediments on Mars have been suggested to be suited for the sequestration and preservation of organic material (Summons et al., 2011). Therefore, sites containing inverted channels were considered as potential landing sites for the ExoMars 2020 rover mission (e.g., Aram Dorsum; Balme et al., 2016) and the chosen Mars 2020 rover mission (Jezero Crater; Goudge et al., 2018). Therefore, terrestrial analogue studies of such sites are critical to understanding the geologic history, depositional environmental and emplacement mechanisms (e.g., Farr, 2004), as well as whether these substrates could have constituted a habitable environment. This analogue site thus presents an ideal opportunity to understand of the preservation potential of past life or its chemical precursors (e.g., reducing versus oxidizing conditions, concentration of biologically relevant elements, presence of total organic carbon (TOC)) of such features. The study furthermore allows a thorough investigation of the formation events of inverted channels as an analogous Martian terrain of interest for future rover exploration. We also discuss the difficulties in detection of past life with the available rover instruments within the context of paleochannel and lacustrine deposits. The following sections detail the methods employed by the on-site field team to acquire the in-sim data, the post-mission laboratory methods for sample analysis, and the science results of those efforts.

3. Field Geology and Laboratory Methods

3.1 Field Methods

The primary focus for the on-site field team was to carry out the science commands from mission control, facilitating the simulation of a fully integrated Mars 2020 rover. The field team, therefore, had the responsibility of carrying out the field analyses of the stand-in, field portable instruments as commanded daily by the Mission Control Team and acquiring a total of eight CanMars drill and push-core (in-sim) samples targeted by the Science Team. The operational scenarios and rationale for choosing the “returned” samples during the in-sim mission are detailed by Caudill et al. (2019). The following sections detail the data acquisition, as well as logistics necessary for operation of the field instruments for CanMars operations. In addition, the field team performed the out-of-sim work (the results of which were not transmitted to mission control) for geologic characterization independent of the mission simulation, which included field mapping, stratigraphic sections, and high-density sampling of representative units in the field area. Samples collected by the field team are divided into three main groups: 1) the eight selected in-sim core samples, including their larger, accompanying duplicates collected when possible; 2) samples from adjacent sites along the rover traverse (e.g., outcrops that were analysed with rover instrumentation but from which in sim samples were not collected); 3) samples from the regional terrain collected for context by the field team. All acquired samples, with description and location information, are provided in Appendix 1 and their locations are shown in Figure 2. Appendix 2 provides the field calibration procedures for the stand-in instruments.

The in-sim data was collected in such a way as to avoid damaging the outcrops in order to minimize human impact on the field site as well as to preserve the fidelity of the simulation. Avoidance of outcrop damage was particularly important during phase two of the mission – a Fast Motion Field Test (FMFT), or rapid data collection period (Pilles et al., 2019). A number of outcrops were revisited several times, presenting the possibility that subsequent outcrop images could reveal out-of-sim disturbance effects. Some site disturbance was necessary, as targeted samples were compacted prior to VIS-IR and pXRF data acquisition. Outcrops were also disturbed by drilling to obtain cores, though as the rover performed this operation autonomously, it was considered in-sim and not of issue to the mission control team. In some rare cases, weather conditions would not allow for in situ data acquisition; in these events, small samples of the target units were collected and analyzed at base camp located ~500 m from the landing site. While this is approach was less favorable in terms of mission fidelity, adverse weather conditions would have resulted in reduced data quality, risk of damage to instrumentation, and/or prevented the practical or safe use of tools in situ.

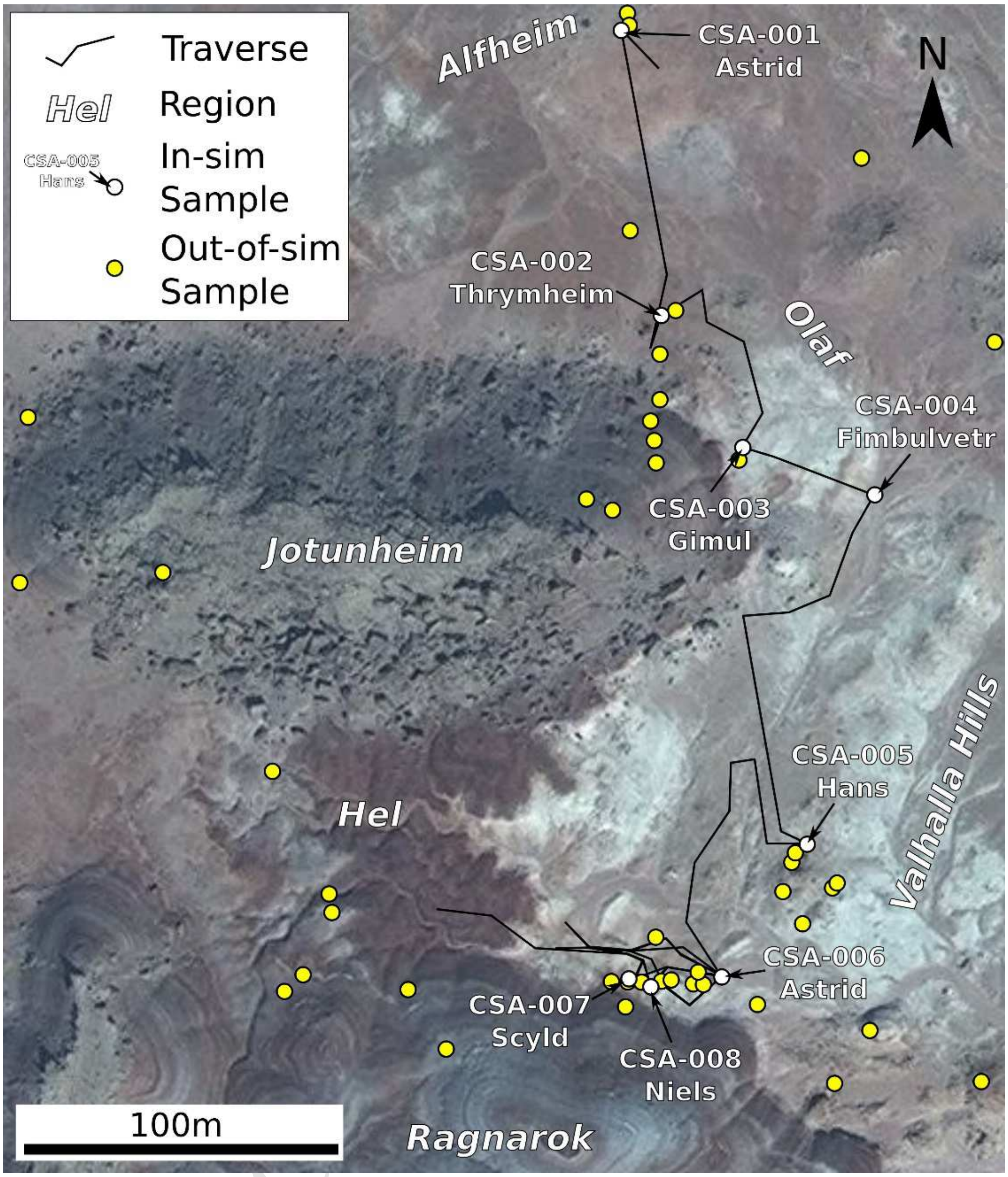

Figure 2. Regional view of the CanMars field site, showing collected samples that were chosen by the in-sim Science Team for "return" laboratory analyses (white circles), as well as samples collected out-of-sim for geologic context and interpretation of the site (yellow circles), further afield than was traversable by the rover.

3.2 Laboratory Methods

X-ray Diffraction (XRD). Rock samples were crushed and powdered via an agate mortar and pestle until sifted through a 500 um sieve. Laboratory X-ray diffraction (XRD) was performed using the Rigaku Geigerflex XRD instrument at Western, operated through MDI Data Scan 5 software package and analyzed from 10–90° 2θ (Co K-α source operated at 160 mA and 45 kV). Mineral phases were identified using the Bruker AXS EVA software package and the mineral database provided by the International Centre for Diffraction Data (ICDD). Powder XRD (pXRD) allows for a confirmation of that mineralogy, directly measuring the basal planes from the mineral structures (including crystalline, poorly crystalline, and poly-crystalline phases) based on peak location, intensity, and pattern shape.

Raman spectroscopy Rock samples were crushed and powdered via an agate mortar and pestle until sifted through a 500 um sieve. Laboratory Raman spectroscopy was performed using a Renishaw Model 2000 Raman at Surface Science Western (785 & 514 nm wavelength), with a range of 140–4000cm^{-1}, a resolution of 1800 l/m grating 2 cm^{-1}, and beam size 2 µm. Raman data was analyzed using Renishaw WiRE software and mineralogy was identified through the RRUFF database (Lafuente et al., 2015). Raman produces a spectrum from a combination of molecular vibrations that is characteristic for given minerals and organic or inorganic compounds.

Visible-Infrared spectroscopy (VIS-IR). Hand samples and powdered samples were analyzed with ASD TerraSpec® Halo portable near-infrared spectrometer in a laboratory setting, capturing spectra in the visible near-infrared (VNIR: 350–1000 nm) and near infrared (NIR: 1001–2500 nm) ranges, with instrument-level white and dark reference calibrations. Corrections for normalizing the spectrum are computed at the instrument-level, as the background is removed by taking the ratio between the reflectance spectrum and the convex hull. First-order matches to mineral spectra were produced via scalars computed from the reflectance spectrum (see ASD TerraSpec specification appendices for scalars and computational methods); spectra were then matched to standards in the USGS spectral library (Clark, 2007) using ENVI Spectral Analyst. Spectral resolution is 9.8 nm at 1400 nm wavelength and 8.1 nm at 2100 nm. The VIS-IR spectral range is beneficial since there are several vibrational modes for common biomolecular chemical moieties (e.g., amide NH bend and stretch, amide and carboxylic acid CO stretch, phosphate OH stretch; Stedwell and Polfer, 2013). This spectral range also specifically indicates elemental bonding indicative of clays, carbonates, and sulfates, all of which are abundant in the field area.

Total Organic Carbon (TOC). Rock samples were prepared at the Astrobiogeochemistry Laboratory at the Jet Propulsion Laboratory (JPL). Samples were cleaned in an ultrasonic bath using 18 MΩ (Millipore) deionized water for ~30 seconds and then dried at room temperature. Samples were ground to a fine powder in an aluminum oxide puck mill that was cleaned between samples with ashed quartz sand, deionized water, and methanol. Powdered rock samples were treated with 1N HCl for 24 hours at 50°C to remove inorganic carbon and then rinsed and centrifuged to neutral pH (3 cycles). Samples were placed in a -20°C freezer for ~2 hours and then transferred to a lyophilizer where they were freeze dried under vacuum at -48°C overnight. 25-30 mg aliquots of sample powders were weighed into tin capsules and analyzed using a Costech 4010 Elemental Analyzer with zero-blank autosampler connected via a Thermo Conflo IV to a ThermoScientific Delta V Plus isotope ratio mass spectrometer. All samples were analyzed in duplicate. Analytical precision is reported as one half the difference between the two individual analyses. Total organic carbon (TOC) was calculated based upon a regression of known mass of C in replicate acetanelide and NBS-19 reference materials versus the area of m/z 44 as determined by the mass spectrometer.

Wavelength Dispersive X-ray Fluorescence spectrometry (WDXRF). Rock samples were powdered via agate mortar and pestle and then pressed into pucks before by heating in a lithium borate flux for sample dissolution. Elemental analysis was performed by a PANalytical PW2400 Wavelength Dispersive X-ray Fluorescence (WDXRF) spectrometer at Western University Geoanalysis Laboratory. WDXRF is a high-resolution elemental detection technique, with typical limits of detections (LOD) <100 ppb.

Optical microscopy. Nikon Eclipse Optical Microscope, LV100 POL compound polarizing microscopes equipped with different combinations of transmitted (TL) and reflecting light (RL) were used for petrography of thin sections. Images were acquired by Nikon DS-Ri1 12 mega-pixel camera.

4. Results

The field assessment provides geologic context of the site further afield than was traversable by the rover. This section describes the results from geological mapping and subsequent sample laboratory analyses. All sample locations are shown in Figure 2 and described in Appendix 1. The geological map produced by the field team is given in Figure 3; corresponding units are referenced throughout the following sections. The stratigraphy documented by the field team is, from bottom to top:

- Pink-buff-colored, medium-grain, calcite-cemented arkosic sandstone, present particularly in the northern field site (unit 8);
- Yellow-buff colored lenticular medium-grain quartz arenite, less than a meter thickness and ten of meters in run-out length, with soft-sediment deformation and local laminar cross beds, and local desert varnish, present in the center of the basin (unit 7);
- White (variably green) bentonite clay-rich siltstone with gypsum lenses (unit 5);
- Laterally discontinuous fine-grained ash matrix tuff with altered glass, mineral grains, and other fragments (unit 4);
- Grey-green-white bentonite clay-rich siltstone with several cm-thick popcorn-textured erosional face and an orange-brown alteration on weathered surfaces; locally finely laminated and with sparse, local tuff outcrops; Lenses of white, fine-grained gypsum and potentially other evaporates weathering out at the surface and tens of cm-scale gypsum veins preserved at several cm depth (unit 3);
- Red-purple bentonite clay-rich siltstone with several cm-thick popcorn-textured erosional face; locally finely laminated with local tuff outcrops. Lenses of white, fine-grained gypsum and potentially other evaporates weathering out at the surface and tens of cm-scale gypsum veins preserved at several cm depth (unit 2);
- Capping unit of coarse-grained, silica-cemented (sparry quartz and chert) conglomeratic sandstone; the capping units of both paleochannel segments in the field area are cross-bedded, with dips indicating paleo-flow towards the north and east (unit 1).

4.1. XRD, Raman, and VIS-IR

Table 2 presents the data from pXRD, Raman, and VIS-IR laboratory analyses. Sample descriptions are provided in Appendix 1, and the spatial bounds and geologic context are provided in Figure 3.

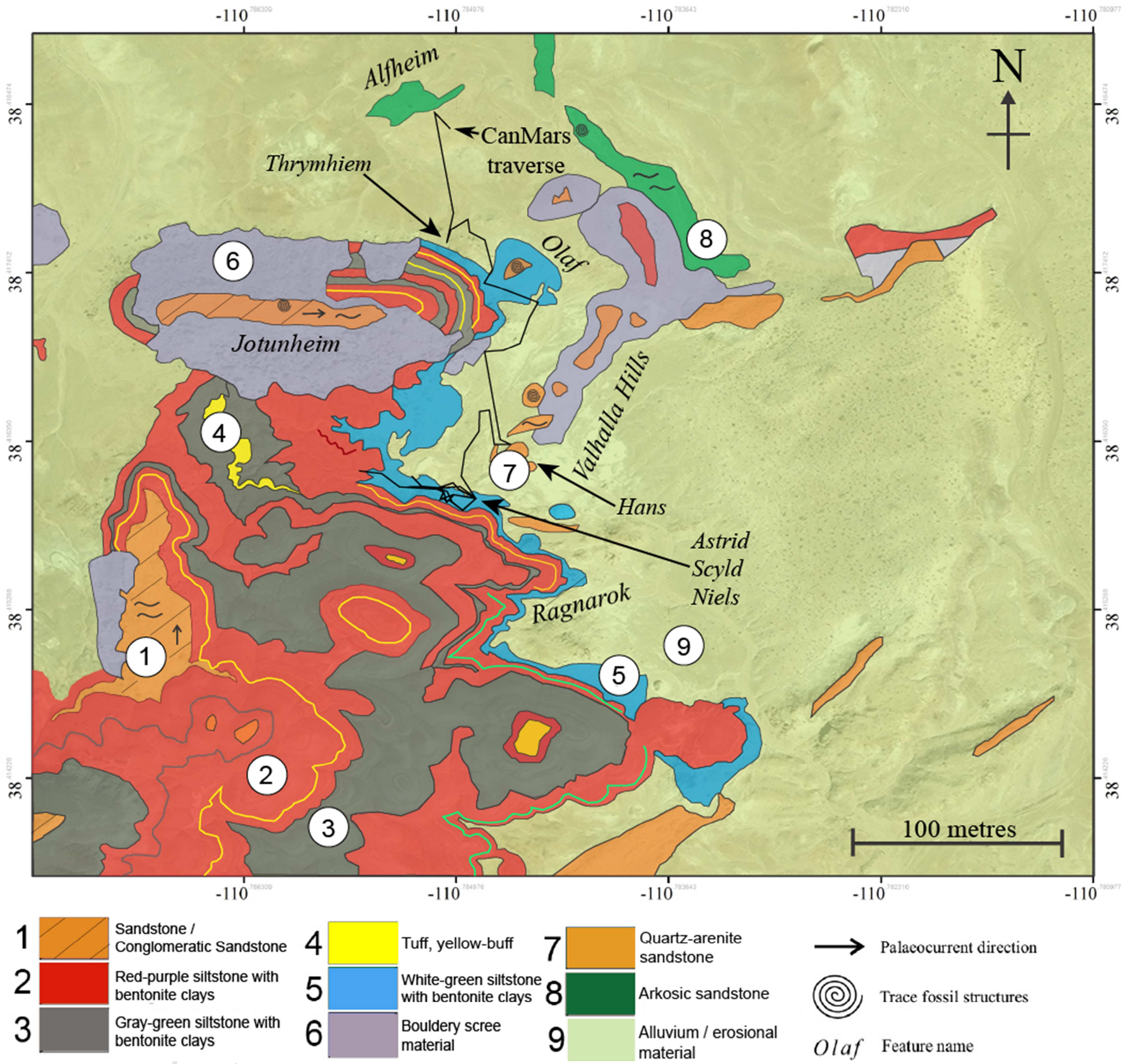

Figure 3. Out-of-sim geologic map at 1:2,500 scale. Numbered units are correlated to samples throughout following sections, with some key target locations listed. Black line indicates the 2015 and 2016 CanMars rover traverse.

The siltstone sequence rocks (units 2 and 3, Fig. 3; Fig. 4a–c) were comprised primarily of montmorillonite (± saponite, vermiculite, and beidellite) and quartz with Fe-oxides, gypsum, calcite, chlorites, and feldspars. The laboratory VNIR-SWIR data show that the siltstone samples are characterized by the presence of ~1.4 μm and ~1.9 μm features, indicating hydration, and ~2.21 μm features, indicative of Al-OH bonds (Fig. 5; Astrid and Scyld samples); due to the width of individual absorptions and the overall shape of the spectra, these are interpreted as the swelling clay montmorillonite based on the close match the USGS spectra. The presence of swelling clays in the siltstones is consistent with the in-sim data and interpretations from the Science Team (e.g., Fig. 6). Swelling clays are common alteration products of higher temperature hydrothermal or volcanic source material (Clay Minerals Society, 2016). the Science Team interpreted the popcorn erosional texture and the presence of montmorillonite as an indication of a volcanic ash-fall component to the unit during emplacement. The presence of gypsum, as seen in the laboratory VNIR-SWIR laboratory data (Fig. 5) and Raman data (Fig. 7), was an important validation from the efforts in-sim to discern the white lenses of material within the siltstone units (Fig. 4c); these lenses and patches of material on the valley floor were local, 10s of cm-scale, and apparently unconsolidated or erosional material. Laboratory XRD and Raman confirmed the presence of sulfates (gypsum) and Ca-phosphates (brushite) in the analyzed field samples (Table 2). Abundant, well-crystallized cm-scale veins of gypsum were observed several cm's below the surface between the grey-green siltstone and red siltstone units (Fig. 8) as well as the black-purple-red siltstone unit. The presence of gypsum indicates that water tables fluctuated during deposition; periods of low water resulted in the formation of evaporites. Fluctuating water tables during the emplacement of these units, and/or during post-emplacement diagenesis, also dictated the physiochemical conditions of the units (e.g., reducing or oxidizing conditions).

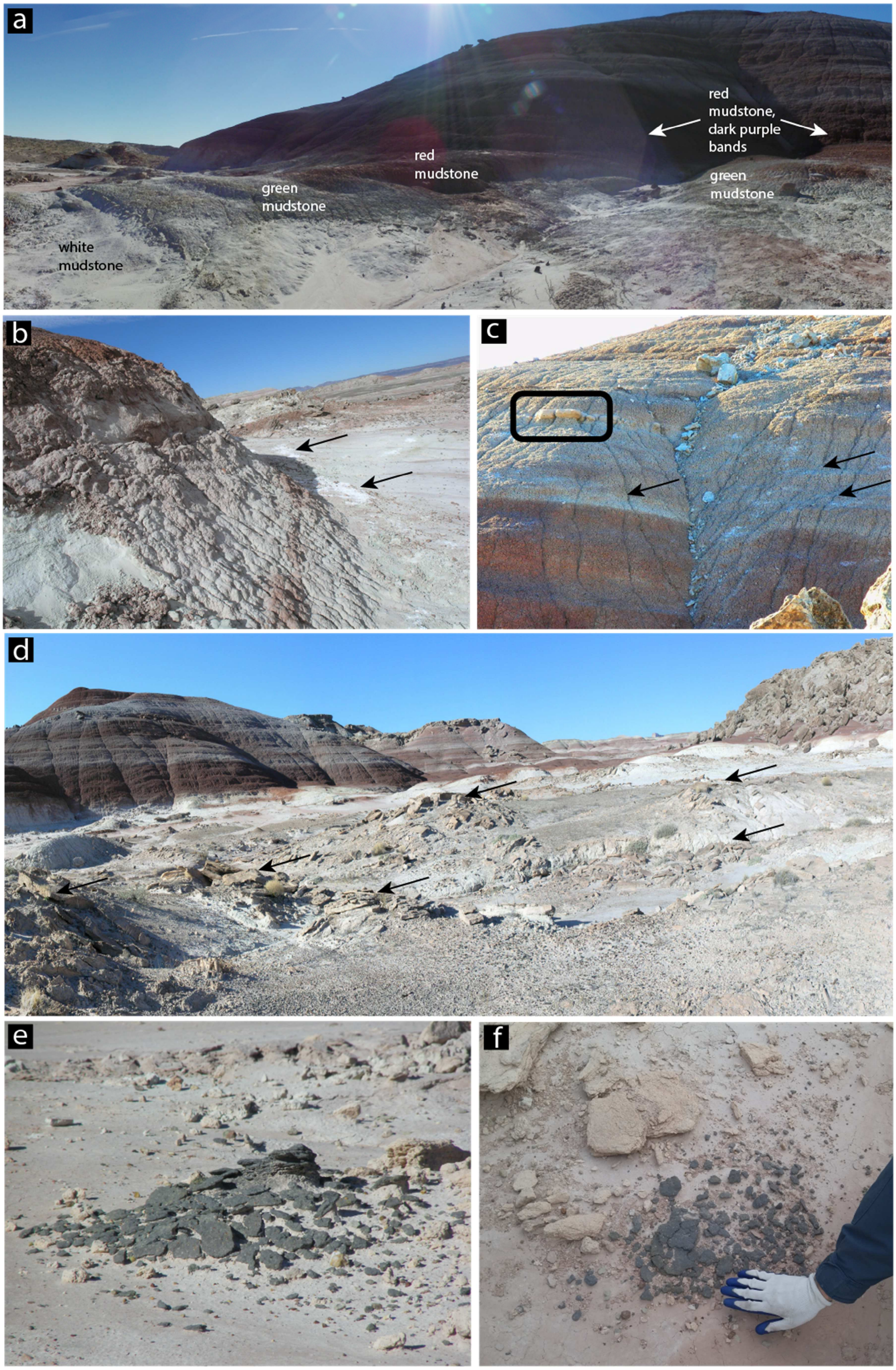
a
red
mudstone,
dark purple
bands
red
mudstone
green
mudstone
green
mudstone
white
mudstone
b
c
d
e
f

361

Figure 4. a) Rover-acquired panorama from the center of the basin, showing multiple lenticular sandstone outcrops (indicated by black arrows). The sandstones are typically <1 m in thickness and meters to tens of meters in length (unit 7, Fig. 3). b) Rover-acquired zoom image of “Gorm” black-green sandstone (unit 3, Fig. 3). c) Photo of “Gorm” taken during the post-mission field visit with hand for scale. d) Rover-acquired panorama showing the lacustrine sequence, shown to highlight the green units. White-green (unit 3, Fig. 3) is overlain by a red-purple lacustrine unit (unit 2, Fig. 3). e) Rover-acquired zoom image of the base of the lacustrine sequence. Note that a disturbance on the surface gives a fresh exposure beneath the several cm-scale shrink-swell erosional outer coating. Black arrows indicate bright white ephemeral patches on the valley floor. f) Rover-acquired zoom image of the base of the lacustrine sequence. Black arrows indicate bright white lenses of gypsum-bearing material throughout all the lacustrine units. Black box indicates the local tuff outcrops, deemed “potatoes,” during the in-sim mission.

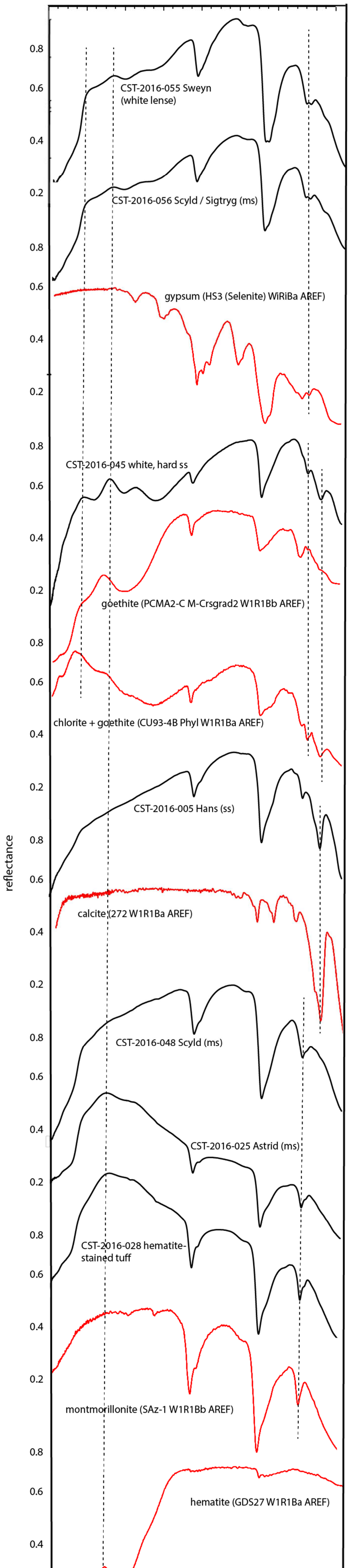

reflectance
0.8
0.6
0.4
0.2
CST-2016-055 Sweyn (white lense)
CST-2016-056 Scyld / Sigtryg (ms)
gypsum (HS3 (Selenite) WiRiBa AREF)
CST-2016-045 white, hard ss
goethite (PCMA2-C M-Crsgrad2 W1R1Bb AREF)
chlorite + goethite (CU93-4B Phyl W1R1Ba AREF)
CST-2016-005 Hans (ss)
calcite (272 W1R1Ba AREF)
CST-2016-048 Scyld (ms)
CST-2016-025 Astrid (ms)
CST-2016-028 hematite-stained tuff
montmorillonite (SAz-1 W1R1Bb AREF)
hematite (GDS27 W1R1Ba AREF)

Fig. 5 Selected laboratory VNIR-SWIR spectra of key and representative samples, shown in black. USGS library spectra (Clark et al., 2007) are shown for comparison. The spectra from the siltstone samples Sweyn and Sigtryg samples suggest a spectral mixing of gypsum, montmorillonite, and an Fe-oxide; the 2.264 µm-centered broad spectral feature and the shape of the spectra in this region maybe be related to the Al-OH and Mg-OH bonds present in gypsum, though likely there is influence from the 2.21 µm feature due to the Al-OH bond in montmorillonite. The Scyld and Astrid siltstone samples show the 2.21 µm feature the strongest, and their spectral shapes match well to that of montmorillonite. We suggest that an Fe-oxide component is present in almost all the sample spectra at ~ 0.35 – 0.80 µm from goethite and hematite; from 0.4 – 1 µm, ferric iron produces an absorption feature due to free ferric ion interaction with surrounding ligands in the crystal. The Hans sandstone sample shows a clear carbonate signature at 2.34 µm and closely matches the spectra shape of calcite.

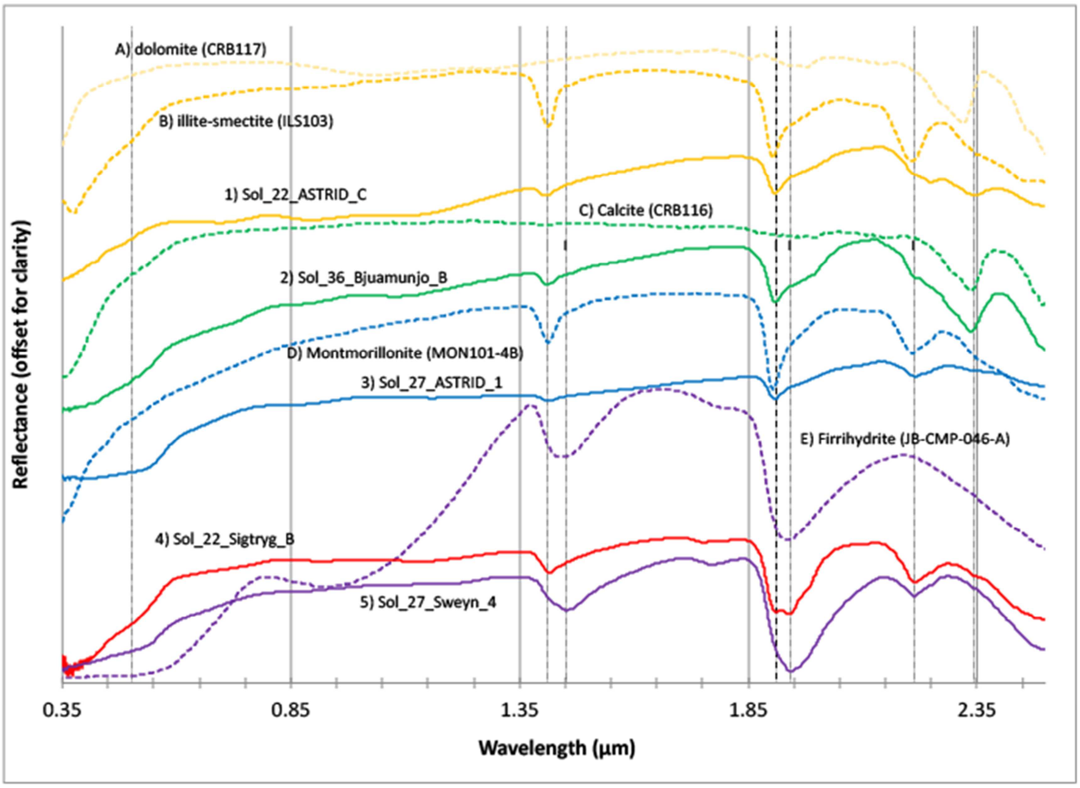

Figure 6. Selected in-sim VIS-IR spectra (solid spectral lines) from the siltstone sequence rocks (units 2 and 3 Fig. 3; Fig. 4a–c) compared to USGS library spectra (dashed spectral lines), matched by shape and position of absorption features. The acquisition sol of each spectra is indicated in the target name. Target Astrid (red lacustrine unit) are presented with matches to illite-smectite (yellow) and montmorillonite (blue); target Bjuamunjo (white-green lacustrine unit) matches to calcite (green spectra); targets Sweyn and Sigtryg (red lacustrine unit; purple and red spectra) matches to ferrihydrite (purple) and montmorillonite (blue).

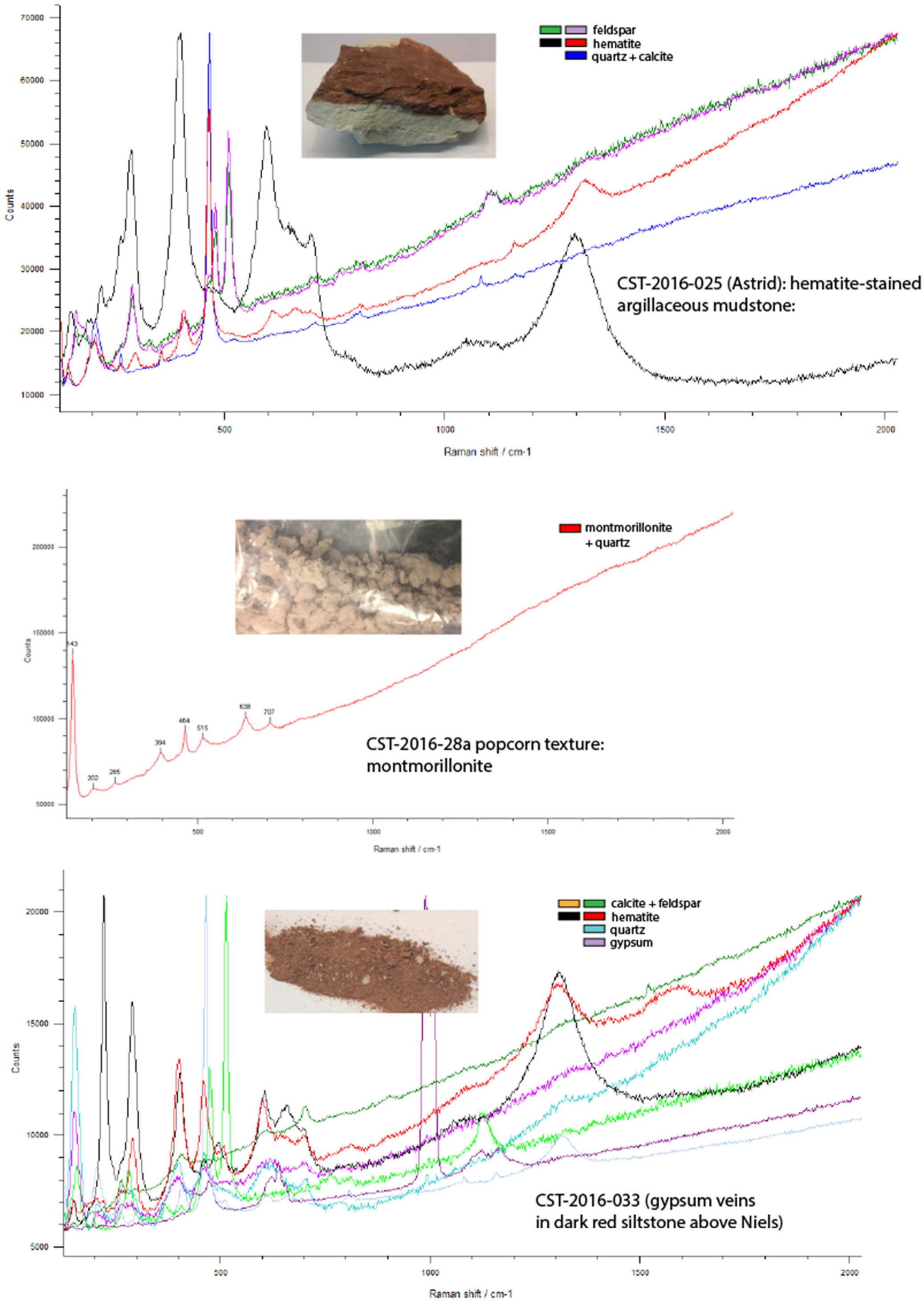

Figure 7. Selected laboratory Raman spectra of key and representative samples of siltstones. a) Astrid (red siltstone unit) is dominated by clays with signatures of hematite. b) The popcorn-

textured erosional material that covers the siltstone units is shown as dominated by montmorillonite with a lesser quartz peak. c) Hematite, quartz, gypsum, and calcite are present in the sandstones.

Figure 8. a) Green finely laminated siltstone sample acquired post-mission. b) The in-sim, rover-derived panorama which captured an outcrop of the finely laminated, green siltstone (indicated by red circle). The small outcrop was not recognized as distinct from the surrounding sandstones and mudstones. c) Well-crystalized gypsum veins and flakes (white), present several cm below the surface, at the contact between the grey-green mudstone and red mudstone units. Pencil for scale. d) At the contact between the grey-green mudstone and red mudstone units, orange

alteration was determined as jarosite, hematite, and goethite based on post-mission laboratory analysis.

Table 2. Mineral phases for samples from pXRD, Raman, and VIS-IR. "CSA" samples indicate the in-sim samples; "CST" indicates samples collected out-of-sim. Sample descriptions are provided in Appendix 1. Named outcrops are given with the corresponding unit from Fig. 3. Lithologies ("lith") are abbreviated as: ss = sandstone; cong = conglomerate; unc = unconsolidated material; m = mudstone; t = tuff. Mineralogy is indicated as: Q = quartz; Plag = plagioclase; Mont = montmorillonite; Ortho = orthoclase; Cal = calcite; Graph = graphite Kf = K-feldspar; Anat = anatase; Hem = hematite; Goe = goethite; Gyp = gypsum. Mineral phases were observed by analyses as indicate by: "X" = XRD; "R" = Raman; (V) = VIS-IR).

ID	lith	outcrop / unit	Q	Plag	Mont	Ortho	Cal	Kf	Anat	Hem	Goe	Gyp	Other
CSA-001	ss	Alfheim, unit 7	R				R						carotene (R)
CSA-002	cong	Thrymhiem, unit 1	R				R						carotene (R)
CSA-003	unc	Gimil	R				R	R	R				
CSA-004	unc	Fimbulvetr	R	R			R						
CSA-005 / CST-2016-005	ss	Hans, unit 7	R, X		V		X	R				V	vermiculite (V), moganite (R), carbon (X)
CSA-006 / CST-2016-025A	m	Astrid, unit 4	R,	X	R, V		R	R, X		R, V			magnetite (X), carbon (X),
CSA-006 /	m	Astrid, unit 4	R,	X	X	X	R	R,		R, V			epidote (V)

CST-2016-025B			X, V					X					
CSA-007 / CST-2016-056	m	Scyld, unit 5	R, X	X	R, V	X		R, X		R, V			amorphous carbon (R), jarosite (V), carbon (X)
CSA-008 / CST-2016-028A	ss	Niels, unit 5			R, V		V					V	rectorite (V)
CST-2015-001	ss	unit 7	R				R	R					
CST-2015-002	ss	unit 7	R	R			R						
CST-2015-003	unc		R				R	R					
CST-2015-015	unc		R	R					R				
CST-2015-016	unc		R	R					R				carotene (R)
CST-2015-019	m	unit 4	R					R	R				
CST-2015-023	unc		R	R			R	R	R	R			carotene (R)
CST-2015-024	unc		R				R	R	R	R			carotene (R)
CST-2015-025	unc		R					R	R				
CST-2015-026	m	unit 5	R				R	R	R				
CST-2016-001	ss	unit 7			V						V	V	Illite (V), Chlorite (V)
CST-2016-002	ss	unit 7								V		V	illite (V), - gmelinite (V), Chlorite (V)
CST-2016-003	ss	unit 7			V								
CST-2016-004	t	unit 4 and 5 contact			V		V					V	epidote (V), vermiculite (V)
CST-2016-006	ss	unit 7			V					V			

CST-2016-007	ss	unit 7			V								illite (V), gmelinite (V)
CST-2016-008	t				V		V						stilpnomelane (V), illite/smectite (V)
CST-2016-009	ss	unit 7			V		V						
CST-2016-010	t	unit 4 and 5 contact	R, X	X	V	X	R	X	R	X			amorphous carbon (R), tourmaline (V), moganite (R)
CST-2016-011	cong	Thrymhiem outcrop, unit 1			V								
CST-2016-012	ss	unit 7			V		V						epidote (V)
CST-2016-013	cong	unit 1			V								
CST-2016-014	ss	unit 7			V							V	rectorite (V)
CST-2016-015	ss	unit 7			V		V						epidote (V)
CST-2016-016	t	unit 4 and 5 contact			V					V			
CST-2016-017	m	unit 4			V					V			
CST-2016-018	ss	unit 7			V					V			
CST-2016-020	m	unit 6											stilpnomelane (V), clinozoisite (V), illite (V), brucite (V), vermiculite (V)

CST-2016-021	cong	unit 1			V							V	illite (V), gmelinite (V)
CST-2016-022	t	unit 4 and 5 contact	R, X	X	X, V	X	R	R, X		R, V	V		rectorite (X), carbon (X) tourmaline (V), moganite (R)
CST-2016-023	ss	unit 7	R, X	X	X, V			R, X		R, V			
CST-2016-024	m	unit 4			V					V			
CST-2016-026	cong	Thrymhiem outcrop, unit 1	R, X		V		R, X	R		V	VV		chabazite (V), moganite (R), illite (V)
CST-2016-027	ss	Alfheim outcrop, unit 7	R, X	X	V		R, X, V						huntite (X), illite-smectite (V), stilpnomelane (V), moganite (R)
CST-2016-029	m	unit 5			V								illite (V), clinozoisite (V)
CST-2016-030	ss	Hans outcrop, unit 7	R, X	R, X	R, V	x	X	X					rectorite (V), clinozoisite (V), moganite (R), cuprite (X)
CST-2016-031	t	unit 4 and 5 contact	R, X		V		R, X	R		R	V		tourmaline (V), cuprite (X)
CST-2016-032	m	unit 6	R,	X	R, V	X	R, X	R					chlorite (V),

			X										clinozoisite (V), vermiculite (V)
CST-2016-033	unc	Niels outcrop, unit 5	R, X	X	X, V	X	R, X	R, X		R, V		R	amorphous carbon (R), carbon (X), palygorskite (V)
CST-2016-034	m	unit 6	R, X	X	X, V		X	R		R			epidote (V), clinozoisite (V), clays (R), cuprite (X)
CST-2016-035	m	unit 4			V								palygorskite (V)
CST-2016-036	m	unit 5			V								illite (V)
CST-2016-037	m	unit 5	R, X	X	X			R, X		R			Ca-fluroapatite, chlorite (V), illite-smectite (V), stilpnomelane (V), cuprite (X)
CST-2016-038	ss	unit 7			V								muscovite (V)
CST-2016-039	ss	unit 7			V							V	rectorite (V), clinozoisite (V)
CST-2016-040	m	unit 5	R, X	X			R						amorphous carbon (R), carbon (X), cuprite (X),

													chlorite (V), vermiculite (V), clinozoisite (V), mognaite (R), stilpomelane (V)
CST-2016-041	t	unit 4 and 5 contact	R, X	X	X, V		R	X		R, V	V		amorphous carbon (R), carbon (X), beidellite (X), tourmaline (V), ulvospinel (X)
CST-2016-042	m	unit 4 and 5 contact			V					V			tourmaline (V)
CST-2016-043	ss	unit 7	R, X		V		R, X, V	R, X				V	illite (V), rectorite (V), vermiculite (V)
CST-2016-044	ss	unit 7											illite/smectite (V), gmelinite (V)
CST-2016-045	ss	unit 7	R, X		V					R		V	illite (V), hematite (R)
CST-2016-046	m	Astrid contact, unit 4	R, X	X	X, V		R, V	x		R, V			amorphous carbon (R)
CST-2016-047	t	unit 4 and 5 contact			V					V	V		illite (V)
CST-2016-048	m	Scyld			V								jarosite (V)

		outcrop, unit 5											
CST-2016-049	t	unit 5			V								illite (V), muscovite (V)
CST-2016-050	m	unit 6			V								illite (V)
CST-2016-051	m	unit 4			V								
CST-2016-052	m	unit 5			V								
CST-2016-053	t	unit 4 and 5 contact			V		V						epidote (V), illite (V)
CST-2016-054	m	unit 5			V								
CST-2016-055	m	unit 4			V					V		V	
CST-2016-057	m	Gorm, unit 6	R, X	X	X, V	X				R			palygorskite (V), moganite (R)
CST-2016-058	m	Niels outcrop, unit 5	R, X	X	X, V					R		x	epidote (V), clinozosite (V), moganite (R), illite (X), cuprite (X)
CST-2016-059	ss	unit 7			V								
CST-2016-060	m	unit 5 / unit 6	R, X				X	R				V	Ca-fluroapatite (X), ferrihydrite? (R), carbon (X) sodalite (X), chlorite (V), illite (V)

CST-2016-061	t	unit 5			V								phengite (V)
CST-2016-062	m	Scyld outcrop, unit 5			V					V			illite (V)
CST-2016-063	unc	Fimbulvetr outcrop			V								muscovite (V)

Localized, white, bulbous outcrops within the lacustrine unit referred to as "potatoes" (unit 4, Fig. 3; Fig. 4c), were hypothesized to be concretions or carbonates by the in-sim Science Team. Figure 9 show the laboratory XRD results of one of the "potato" samples, which is comprised of quartz, plagioclase feldspars, montmorillonite, beidellite, and ulvospinel. Laboratory Raman further indicated the presence of anatase and plagioclase in these samples (Table 2). The VNIR-SWIR spectral results indicate an Fe-oxide contribution at ~ 0.80 μm (Fig. 5) due the free ferric ion interaction with surrounding ligands in the crystal. Maghemite (γ-Fe_2O_3) was identified in Raman data, which is formed by low-temperature weathering or oxidation of ferrous spinel, commonly titanium magnetite. These are common tuff mineral assemblages, particularly anatase and the titanomagnetite ulvospinel.

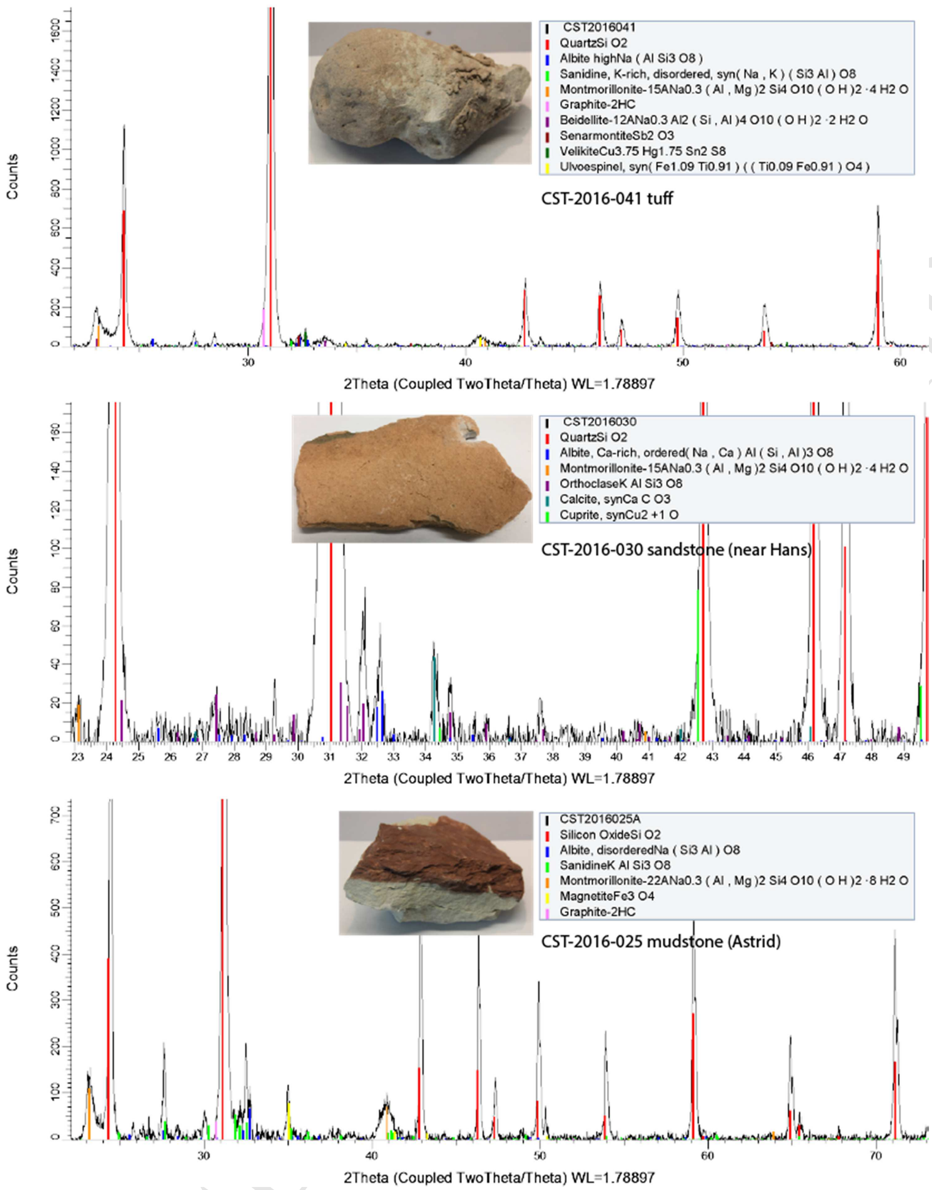

Fig. 9. Selected laboratory XRD patterns of key and representative samples of tuff, sandstone, and mudstone. Montmorillonite (with a strong low 2-theta 001 peak) and quartz (the tallest peaks, having the highest counts) are the dominant mineralogy signatures in all samples. The CST-2016-041 sample has mineralogy consistent with a tuff, including plagioclase and ulvospinel. Sample CST-2016-030 is a typical sandstone of the braided channel system in the

basin with quartz, feldspars, calcite, and clays. The siltstones (represented by Astrid CST-2016-025) have similar mineralogy, excluding carbonates.

The lenticular sandstones in the basin are comprised of quartz, feldspars, gypsum, calcite, montmorillonite, and ferric iron phases. Figure 10 shows example Raman spectra of varying mineralogy of two generations of sandstones; the younger arkosic sandstones (e.g., Hans; unit 7, Fig. 3) are silica cemented, and the older quartz arenite sandstones (e.g., Alfhiem, unit 8, Fig. 3) are calcite cemented. Laboratory VIS-IR data also commonly show what are interpreted as Fe-oxide (~ 0.80 μm feature) and montmorillonite (~ 2.21 μm feature) components (Fig. 5).

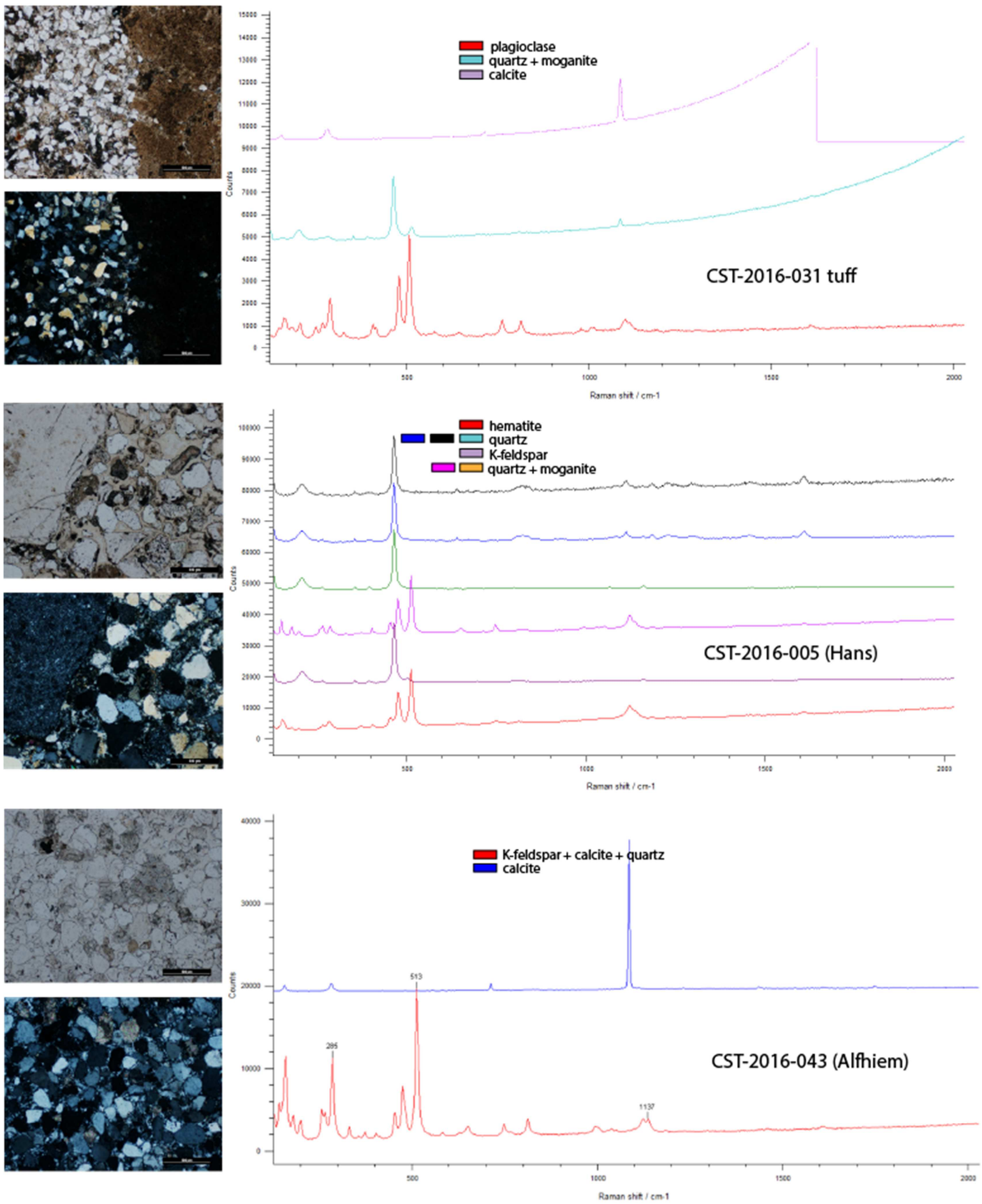

Figure 10. Selected laboratory Raman spectra of key and representative samples of tuffs and sandstones. Pictomicrographs are shown for context PPL (upper images) and XPL (lower images); all scale bars are 500µm. a) Tuff samples were dominated by plagioclase in Raman spectra, with quartz and moganite. The petrography shows altered glass and mineral grains (see Fig. 11 for detailed pictomicrograph descriptions). b) Hans sample, a younger silica cemented

sandstone; petrography shows texturally and compositionally different fragments. c) Alfhiem is interpreted as a calcite-cemented quartz arenite sandstone.

4.2. TOC

Solvent extraction Gas Chromatography Mass Spectrometry (GC-MS) showed that the sandstones had the highest TOC of the in-sim cached samples, but the level of TOC (at <0.03 wt%) was 100 times less than is considered organic-rich for sedimentary rock (Boggs, 2006). The green and red lacustrine units (i.e., Neils and Astrid) showed TOC values at 106 ppm (or 0.01 wt%). The conglomerate sample from the capping unit was chosen as the third priority for sample return in-sim yet showed the highest TOC of all samples in the field site (237 ppm). The next highest was Hans, a lenticular sandstone in the center of the basin which represents an ancient braided channel system, stratigraphically below the lacustrine sequences of the inverted paleochannel. Following the conglomerate and the sandstone, the green laminated siltstone lithologies had the next highest TOC. The 6th highest was then Neils, the green-gray mudstone, which was chosen as highest priority for sample return by the in-sim Science Team.

Table 3. TOC abundances. “CSA” samples indicate the in-sim samples. MSRAD refers to equivalent units in the independent site field validation performed by Beaty et al. (2019). Units described with the outcrop names refer to the geologic map in Fig. 3. Sample descriptions are provided in Appendix 1.

sample ID	TOC (ppm)	± (ppm)	outcrop / unit	description	in-sim sample return priority
CSA-005 / CST-2016-005	260	2	Hans, unit 7	Sandstone	4

CST-2016-010	55	5	unit 4	Fe-stained tuff	
CST-2016-022	39	1	unit 4	Fe-stained tuff	
CST-2016-023	40	1	unit 8	Arkosic Arenite	
CSA-006 / CST-2016-025	46	3	Astrid, unit 2	red/purple siltstone	2
CST-2016-026	237	12	Thrymhiem outcrop, unit 1	clastic sandstone (cap unit)	3
CST-2016-027	101	6	Alfhiem outcrop, unit 2	sandstone, northern site	
CST-2016-030	193	9	unit 7	sandstone, center of basin	
CST-2016-031	47	14		regolith sample	
CST-2016-032	22	4	unit 4	Fe-stained tuff	
CST-2016-033	80	8	unit 2	gypsum vein in purple-red siltstone	
CST-2016-034	52	10	not observed in-sim	green siltstone	
CST-2016-037	55	4	not observed in-sim	green siltstone; out of sim “bed marker”	
CST-2016-040	27	12	not observed in-sim	green siltstone; out of sim “bed marker”	
CST-2016-041	49	1	within unit 2	Tuff	
CST-2016-043	35	1	unit 7	quartz arenite with concretion	
CST-2016-045	44	1	unit 7	sandstone, center of basin	
CST-2016-046	106	27	Astrid (representative contact), unit 2	contact white/red/green siltstone	2
CSA-007 / CST-2016-056	33	6	Scyld, unit 3	green siltstone	7
CST-2016-057	118	14	Gorm, unit 3	black-green sandstone	
CST-2016-058	112	18	Neils outcop, unit 3	green siltstone	1
CST-2016-060	154	15	not observed in-sim	green strongly laminated siltstone	

4.3 WDXRF

Wavelength Dispersive X-ray Fluorescence (WDXRF) spectrometry was used to determine the elemental composition of samples and serve as a laboratory-based control and comparison to the in-sim XRF-derived geochemical data. Quantitative WDXRF geochemical results for the in-sim and out-of-sim samples are provided in Table 4. The in-sim sample Scyld (CSA-007 / CST-2016-056) is deplete in Fe compared to the other lacustrine samples. The samples most enriched in Fe_2O_3 are the mudstones and siltstones, at 2 – 5 wt%, with the highest being the green siltstone sample CST-2016-037. This sample was also the high in P_2O_5 (0.94 wt %). Another green finely laminated siltstone sample (CST-2016-060) also had very high Fe and P (1.40 wt%) relative to the other samples. Scyld was found to have 1.24 wt% Fe_2O_3; samples <1.5 wt% Fe_2O_3 are largely sandstone and conglomerate samples.

Table 4. Quantitative WDXRF geochemical results. "CSA" samples indicate the in-sim samples. All values are provided in weight percent. Sample descriptions are provided in Appendix 1.

Sample ID	SiO_2	TiO_2	Al_2O_3	Fe_2O_3	MnO	MgO	CaO	K_2O	Na_2O	P_2O_5	BaO	SrO	LOI	Total
CSA-001	68.8	0.07	1.12	0.34	0.26	0.37	15.80	0.59	0.17	0.04	0.02	0.01	12.68	100.2
CSA-002	94.1	0.08	1.13	0.46	0.01	0.27	1.27	0.40	0.22	0.10	0.06	0.01	2.06	100.2
CSA-003	80.2	0.23	4.65	0.96	0.15	0.81	4.75	1.42	1.05	0.05	0.06	0.013	5.82	100.1
CSA-004	92.3	0.09	1.86	0.77	0.07	0.38	2.77	0.77	0.32	0.05	0.04	0.012	0.78	100.2
CST-2015-015	72.7	0.54	11.08	2.16	0.02	1.80	0.63	2.88	1.64	0.12	0.04	0.02	6.64	100.2
CST-2015-016	94.1	0.09	2.00	0.35	0.03	0.27	0.74	0.85	0.39	0.04	0.07	0.009	1.23	100.1
CST-2015-019	71.2	0.42	10.64	2.83	0.02	1.96	1.45	1.79	1.43	0.10	0.04	0.032	8.05	100.0
CST-2015-023	81.4	0.41	6.06	1.44	0.05	0.88	2.12	1.80	1.39	0.11	0.07	0.026	4.25	99.9
CST-2015-024	82.2	0.23	5.29	0.91	0.05	0.92	2.59	1.51	1.42	0.06	0.06	0.022	4.67	99.9
CST-2015-025	81.7	0.47	7.02	1.67	0.02	0.83	1.66	1.81	1.24	0.10	0.09	0.031	3.45	100.1
CST-	80.0	0.25	5.17	0.81	0.11	0.94	3.95	1.55	1.45	0.06	0.05	0.011	5.61	99.9

2015-026														
CST-2016-005	94.6	0.08	1.27	0.28	0.02	0.26	1.16	0.33	0.26	0.30	0.02	0.006	1.82	100.4
CST-2016-010	80.1	0.30	9.20	1.51	0.03	1.40	0.76	1.04	1.15	0.04	0.10	0.026	7.24	102.9
CST-2016-022	81.7	0.28	8.04	1.55	0.02	1.23	0.68	1.00	1.02	0.04	0.17	0.025	6.18	101.9
CST-2016-023	85.8	0.32	5.67	1.17	0.05	0.76	1.03	1.21	0.86	0.05	0.56	0.041	3.96	101.4
CSA-006 / CST-2016-025A	80.5	0.40	9.46	1.72	0.03	1.17	0.39	2.49	1.31	0.18	0.03	0.007	5.25	103.0
CST-2016-025B	76.1	0.45	10.40	2.88	0.03	1.37	0.44	2.78	1.29	0.19	0.03	0.009	5.72	101.7
CST-2016-026	97.7	0.04	0.92	0.27	0.02	0.23	0.71	0.27	0.19	0.11	0.00	0.003	1.92	102.4
CST-2016-027	69.4	0.05	1.08	0.28	0.27	0.32	15.95	0.52	0.27	0.05	0.01	0.009	14.27	102.5
CST-2016-030	94.3	0.12	2.17	0.35	0.02	0.33	0.49	0.85	0.34	0.03	0.07	0.006	3.88	103.0
CST-2016-031	78.2	0.20	4.48	0.56	0.58	0.56	6.72	1.32	0.69	0.04	1.45	0.058	7.64	102.4
CST-2016-032	88.8	0.16	4.25	1.87	0.03	1.86	0.45	0.94	0.57	0.05	0.36	0.020	2.60	101.9
CST-2016-033	74.9	0.42	9.59	2.76	0.02	1.33	0.49	2.57	1.93	0.17	0.02	0.011	7.92	102.2
CST-2016-034	88.0	0.21	5.04	1.81	0.07	1.76	1.04	1.00	0.68	0.07	0.22	0.014	3.49	103.4
CST-2016-037	79.6	0.21	5.72	5.17	0.05	3.54	1.58	0.81	0.59	0.94	0.35	0.020	3.87	102.5
CST-2016-040	87.9	0.16	4.31	3.27	0.06	2.49	0.91	0.70	0.47	0.14	0.35	0.014	3.26	104.0
CST-2016-041	80.2	0.27	8.02	1.61	0.02	1.29	0.57	0.90	1.14	0.03	0.16	0.022	6.61	100.9
CST-2016-043	90.6	0.04	1.20	0.16	0.05	0.25	4.48	0.60	0.28	0.04	0.13	0.009	4.81	102.6
CST-2016-045	97.0	0.04	0.98	0.60	0.03	0.25	0.46	0.35	0.30	0.06	0.19	0.065	1.41	101.7
CST-2016-046	76.7	0.23	5.19	0.90	0.21	0.77	6.61	1.37	1.09	0.06	0.06	0.014	7.65	100.8
CSA-007 / CST-2016-056	88.6	0.23	4.69	1.24	0.02	0.51	0.45	1.55	0.71	0.09	1.29	0.060	3.14	102.5
CST-2016-057	91.6	0.14	4.07	0.69	0.03	0.56	0.27	1.22	0.65	0.05	0.07	0.006	1.92	101.2
CST-2016-058	73.2	0.50	11.12	2.27	0.02	1.41	1.05	2.65	1.19	0.19	0.05	0.027	6.65	100.4
CST-2016-060	81.4	0.19	4.63	2.97	0.06	2.47	2.95	0.65	0.47	1.40	0.48	0.025	3.51	101.2

4.4. Petrography

A powerful analytical technique not available to Mars rover teams, but fundamental to the Earth sciences, is optical microscopy of petrographic thin sections. The nearest analogue to traditional petrography of the CanMars instrument suite was the Microscopic imaging with the Three-Dimensional Exploration Multispectral Imager (TEMMI; Ryan et al., 2016; Bourassa et al., 2019), which had a maximum resolution of 2.2 μm per pixel. Petrographic classification of hand samples indicated a general textural and compositional maturity, dominated by quartz and feldspar grains which were rounded and well-sorted (Fig. 11). Sandstones and conglomerates show typical compositions of 85% quartz (monocrystalline, chert, and polycrystalline), 14% matrix (quartz cement, mud, or calcite cement), 1% feldspar (K-feldspar or plagioclase), ± calcite and hematite, and are moderately porous (e.g., Fig. 11a–d). The petrographic data supports the mineralogy obtained from laboratory XRD (Fig. 10); the stratigraphically younger silica-cemented sandstones are classified as arkosic sandstones (e.g., Hans; unit 7, Fig. 3) and the older silica cemented sandstones are classified as quartz arenite sandstones (e.g., Alfheim, unit 8, Fig. 3). Mineral overgrowths in the matrix and pore-filling spaces of the sandstones indicates post-emplacement diagenetic silica, calcite, clays, and gypsum, though differentiating between early and late diagenesis, including possible dissolution and re-precipitation during late diagenesis, is difficult. Sandy lenses within the conglomerates were classified as sublitharenite and are highly porous; the sandstones range from quartz-arenite to arkosic. The tuffs are comprised of altered glass and mineral grains of various sizes, ranging from 100–1000 μm, set in a fine-grained, non-welded ash matrix (Fig. 11e–f). Altered glasses and fine-grained ash comprise roughly 60% of the sample.

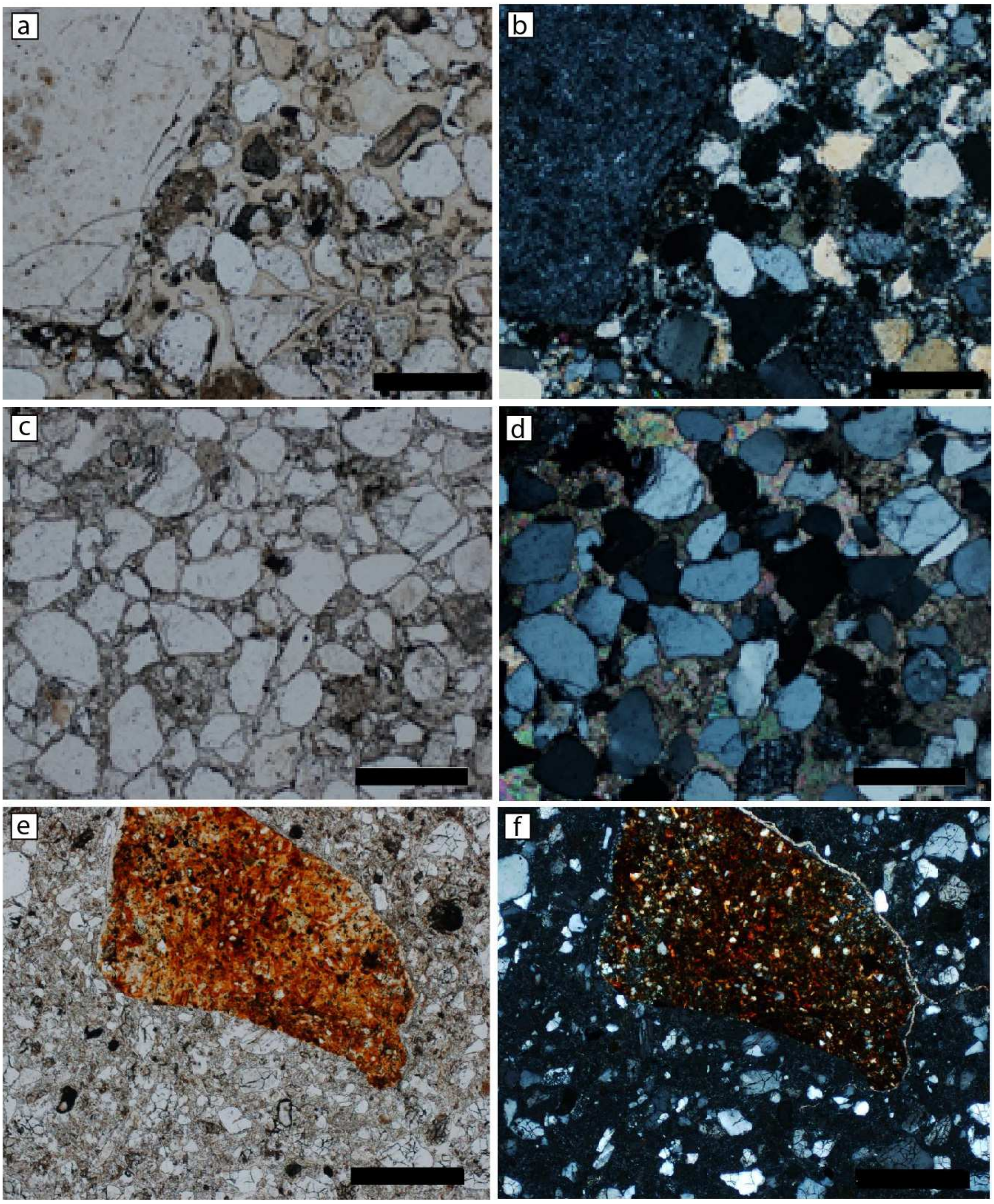

Figure 11. a and b) Thin section of CST-2016-005 (target Hans) in PPL (a) and XPL (b). All scale bars are 500μm. Classified as subarkosic sandstone, clasts are 100-400 μm comprised of

polycrystalline quartz (81%) with chert and mudstone lithics. Monocrystalline quartz comprises the majority of the clasts with a few scattered grains feldspar grains having tartan twinning. Quartz-cemented. Roundness: angular to well rounded; Form: low to high sphericity; Sorting: poorly sorted. c and d) Thin section of CST-2016-027 (from outcrop Alfhiem) in PPL (c) and XPL (d). Classified as quartz arenite sandstone, clasts are 100-600 μm monocrystalline quartz with larger chert lithics, bound by calcite cement. A few grey K-feldspar grains display albite twinning. Roundness: angular to well rounded; Form: low to high sphericity; Sorting: moderately sorted. e and f) Thin section of CST-2016-041 in PPL (e) and XPL (f). Non-welded tuff, with several different texturally and compositionally different fragments; altered glass and mineral grains, 100-1000 μm grain sizes, are set in a fine-grained ash matrix. Altered glasses and very fine-grained ash comprise roughly 60% of the sample (glasses are colorless to light brown in PPL, black in XPL).

5. Discussion

5.1. Comparison of rover-based interpretations to field and laboratory results

In general, laboratory analyses in this study were consistent with the in-sim “rover” data-derived lithological interpretations and supported the in-sim Science Team’s fluvial-lacustrine depositional model. It is notable that remote operations provided a characterization of the geologic context of a fluvial and lacustrine-dominated system (fulfilling MEPAG Goals I and III; McLennan et al., 2012). The following sections offer a detailed comparison of the in-sim science, interpretations, and hypotheses and the findings of the laboratory analyses.

5.1.2 Mudstone units

Based on the rover-derived imagery, the in-sim Science team found that the multi-colored siltstones through the field site had the same shrink-swell erosional characteristics, known as popcorn texture, indicating the presence of high-moderate temperature clays (Clay Minerals Society, 2016). Geochemical data from the rover-acquired XRF instrument showed Fe/Si ratios higher than 2.5 in the erosional regolith and the siltstone units, which supported a high-temperature origin (Fig. 12d; Van Daele et al., 2014). Data from the XRF instrument plotted on an Al-Si-Ca ternary diagram shows that the lacustrine units are argillaceous mudstones (Fig. 12a), which are typically comprised of fine-grained clays, particularly kaolinite, montmorillonite, illite, and chlorite. Figure 12b also shows an A-CN-K diagram with data from the lacustrine unit suggesting a smectite-illite composition. The VIS-IR and Raman instruments provided excellent complementary data suites in an environment that proved to be clay-dominated with lenses of sulfates. Smectite clay mineralogy within all analyzed lacustrine units, as well as in the mixed regolith on the basin floor, was interpreted from the absorption features present in the VIS-IR data (~1.4 μm and ~1.9 μm hydration features, and 2.21 – 2.32 μm features, indicative of Al, Fe, and Mg-OH bonds; Fig. 6). Argillic alteration of volcanic glasses from ash fall into aqueous environments is a common result of diagenesis of the volcanic assemblages to smectite clays (e.g., Compton, 1991), and the team observed no evidence of hydrothermal alteration. The erosional texture, mineralogical, and geochemical evidence, as well as the depositional environment as inferred from the depositional model, led to the interpretation of this unit as having formed in a lacustrine environment with a volcanogenic component; hypothesized to be a regular influx of volcanic ash. The unit was further interpreted to have a very low to zero energy depositional setting with alternating changes in redox state shown by variable Fe-oxide precipitation and thus color variation throughout the unit.

The laboratory analyses confirmed the argillaceous classification of the siltstone units (Fig. 12a). In situ rover-derived mineralogy was also confirmed, including the gypsiferous nature of lenses within the mudstones, indicating a variable water table and intermittently arid conditions. Smectites dominantly comprise the mineralogy of the mudstones (Table 2). Rover-derived kaolinite, muscovite, and mixed-layer montmorillonite-illite were also confirmed through laboratory analysis (e.g., Fig. 12b; Table 2). Based on an in-sim detection of Fe-oxyhydroxide (ferrihydrite) using the VIS-IR instrument, the Science Team hypothesized that such minerals indicated Fe^{3+}/Fe^{2+} redox coupling, formed through microbially-mediated (early) diagenesis in seasonally anoxic lakes (Caudill et al., 2019; Fortin et al., 1993); abiotic dissolution and reprecipitation of Fe-oxides was also considered a likely formation pathway. Goethite, another Fe-oxyhydroxide, was confirmed in laboratory analyses of many of the mudstone samples (Table 2), along with the Fe-oxide hematite; microbially-mediated diagenesis has been shown to transform goethite to hematite under oxic conditions (Das et al., 2011), providing support to the rover team's hypothesis that the diagenetic water chemistry varied from oxic (under oxidizing conditions) to anoxic (under reducing conditions).

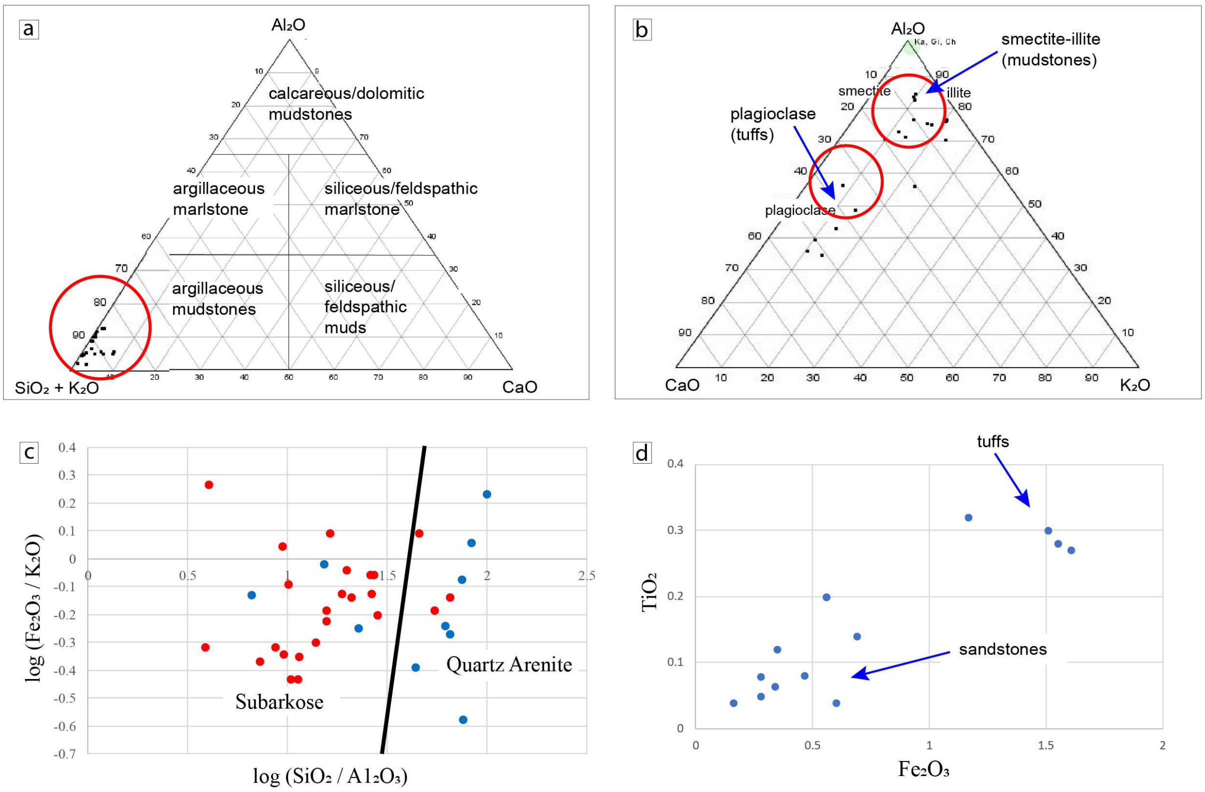

Figure 12. a) Mudstone classification chart overlain with WDXRF laboratory data (black points) from the lacustrine units. Red circle indicates the overlapping field of the in-sim XRF data. Both datasets indicate an argillaceous mudstone composition. b) Alkalis ternary diagram with WDXRF laboratory data from tuff and mudstone samples plotted (black points). Red circles indicate the largely overlapping field of the in-sim XRF data. Both datasets indicate a feldspar composition of the tuff samples (known as “potatoes” in-sim) and smectitic composition for the mudstone units. c) WDXRF laboratory data (blue points) and in-sim XRF and LIBS-acquired data (red points) overlain on log (Fe_2O_3 /K_2O) versus log (SiO_2 /Al_2O_3) plot showing sandstone classifications (after Herron, 1988). d) WDXRF laboratory data displayed in an X/Y plot, highlighting the geochemical differences between the sandstone and tuff samples.

5.1.1 Sandstone units

The sandstone in the area of operations has abundant soft-sediment deformation features and occasionally displays planar cross-beds and are overlain by a less resistant pebble-rich siltstone. The lenticular sandstone units are typically <1 m in thickness and meters to tens of meters in length (Fig. 4d). One geologic hypothesis from the pre-mission data was that the area was the site of an ancient inland sea, which was followed by regression and then emplacement of a lacustrine unit; the sandstones in this scenario would represent a near-shore marine facies. However, the halite or other markers of shallow sea environments were not documented during the mission. Furthermore, the lenticular morphology and braided nature of the sandstones, coupled with sedimentary structures, strongly suggested that the sandstones were fluvial and not shore-line facies. The crossbedding observed in the lenticular sandstone outcrops (as well as the conglomerate capping unit) is a sedimentary structure that indicates stream flow.

Geochemical sediment maturity, sandstone classification plots, and X-Y trends, along with stratigraphic superposition, indicated multiple paleochannel generations. The quantitative elemental data (in-sim XRF and laboratory WDXRF) was used to geochemically classify sandstone samples (e.g., Fig. 12); classification schemes are based on clast and interstitial matrix texture, elemental composition, and mineralogy (e.g., Fig. 11a–d) informing provenance, depositional environment, and diagenetic processes. During the simulation, TEMMI images allowed for determinations of grain size and texture and led to the interpretation of the basal sandstone as being a quartz arenite (Fig. 12c). XRF-derived data indicated that these sandstones were carbonate-rich, and the light-toned cement was interpreted by the Science Team as calcite. It was unclear if the calcite cement was primary or diagenetic. The majority of the sandstones nearer the center of the basin, which comprised the majority of the sandstones in the field area, were interpreted as silica-cemented arkosic sandstones based on the shift in geochemical ratios from the basal sandstones (Fig. 13a). Based on grain size and texture, the Science Team interpreted the sandstones as having been deposited in a medium energy fluvial setting; the late-present oxidizing environment was evidenced by a local, thin, dark Mn- and Fe-oxide rich weathering product known as desert varnish. This was determined based on locally enriched Mn-oxides and Fe-oxides (e.g., Fig. 13c) present as dark coatings on the sandstones. Although geochemical data proved vital to understanding the depositional environment, there were limitations that required supportive data for interpretations. The XRF instrument used was not capable of detecting Na, for example, thus it was difficult to provide evidence of salinity or concentration of elements by evaporative processes; various diagnostic elements (e.g., S, P, Br) might have been below the XRF limits of detection.

Signatures of β-carotene are observed in the sandstones (Table 2), which is a carotenoid pigment present due to past (or present) endolithic life, confirming several in-sim Raman observations of β-carotene in the sandstones. Fe- and Mn-oxide “desert varnish” is present on weathered sandstone surfaces (Table 4; Fig. 13c); both in-sim and field teams recognized this material as indicative of a present-day arid and oxidizing environment.

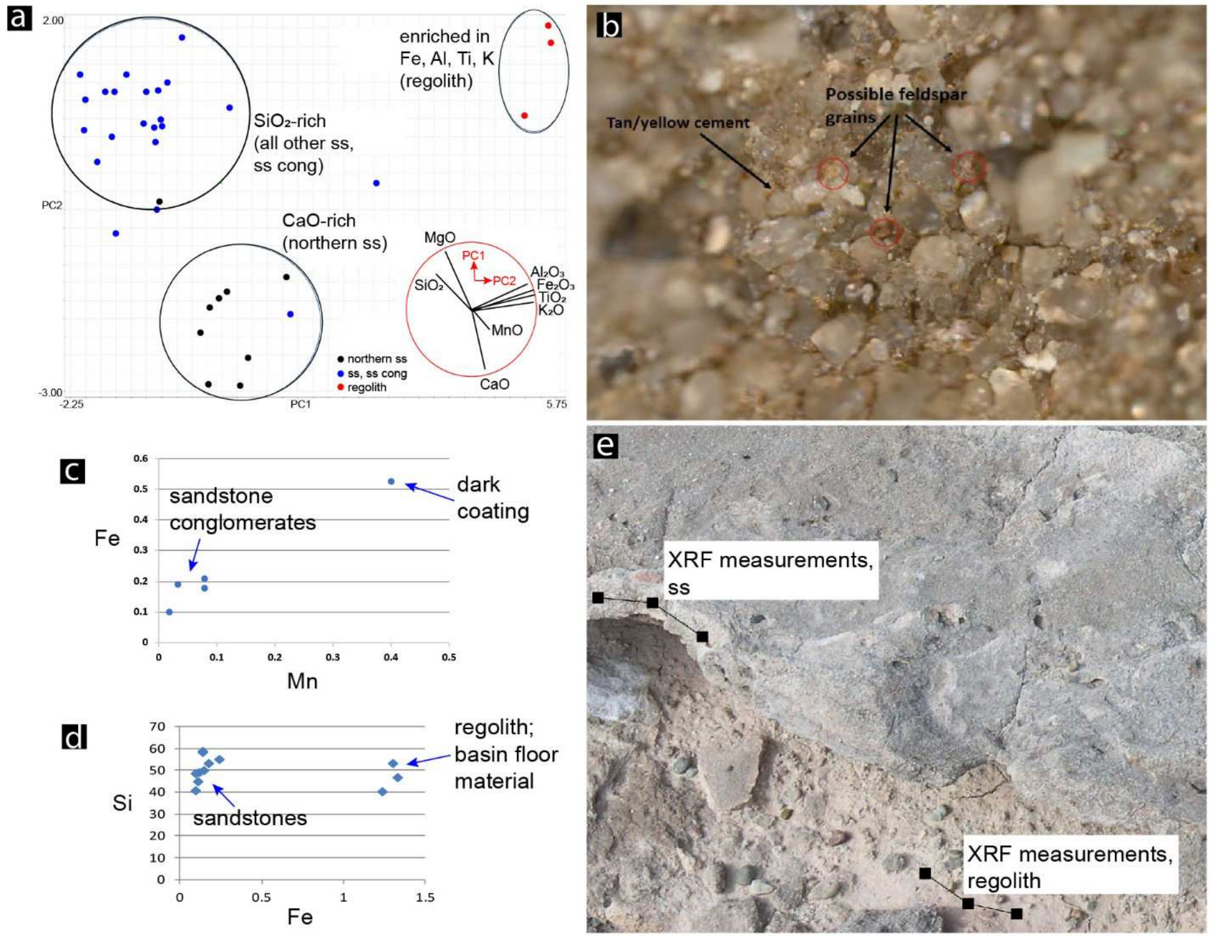

Figure 13. a) XRF-acquired geochemical data from sandstones and regolith is represented in a PCA diagram to display geochemical trends. Oxides are shown on the bottom right with their relative direction of increase and relative weight. The sandstones which dominated the basin were geochemically distinct from the sandstone outcrop in the northern area of the field site; these are both distinct from the geochemistry of the regolith. b) TEMMI image of a quartz arenite, showing dominantly quartz clasts (~95%) with potential feldspars which are poorly sorted. Grain morphology is sub-rounded with a medium sphericity (0.7), and grains 0.1 – 0.4 mm in size, c) XRF-acquired geochemical data displayed in an X/Y plot, highlighting the increase in the Mn/Fe ratio seen in the dark coating of the sandstone (interpreted as Mn- and Fe-oxide rich desert varnish) versus the sandstones. d) XRF-acquired geochemical data showing the

Fe/Si variances between the sandstones and regolith, indicating a volcanic influence in the mineralogy of the regolith. e) An example of XRF measurements planned for acquisition on a sandstone and local regolith.

In summary, the CanMars analogue mission was successful in achieving two of the main goals of the exercise; namely to assess the paleoenvironmental habitability potential and history of water at the site and characterize the geology (Caudill et al., 2019). The field and laboratory validation work documented here suggests that the in-sim instruments were adequate to characterize samples. However, it is clear that rover-based field work is hampered by mobility and time constraints as compared to a human field geologist. This has an obvious effect on efficiency but also precision, and to some extent, accuracy. Some important details were missed by the in-sim rover team due simply to lack of mobility, terrain access, and image exposure and perspective. A key benefit of an analogue exercise is the capability to physically visit the site for confirmation of the remote geologic assessment. The field team's documentation of the details missed by the rover Science Team is discussed in the following section.

5.2. Field team and laboratory observations not captured by the in-sim Science Team

One immediately obvious lesson to the Science Team during the post-mission field visit was that the sense of scale was generally not appreciated. Even though the scale of imagery was known, and LIDAR and terrain visualization software were available, the true sense of location and relation of the rover to outcrops, formations, and traversable areas remained abstract to the

Science Team; this speaks the inherent problem in conceptualizing and discerning scale in rover missions, which has been noted with previous analogue missions (e.g., Antonenko et al., 2013).

The in-sim Science Team was not able to identify the isolated tuffs (white, bulbous lithologies referred to as "potatoes") that were sparsely present throughout the lacustrine units but were able to discount the hypothesis that they were carbonates based on the *in situ* data returned. The petrography and mineralogy presented in this study is consistent with this lithology as being volcanic tuff, having a fine-grained ash matrix, and altered glasses and very fine-grained ash which comprises roughly 60% of the sample with few scattered, angular fragments. (Fig. 116–f). Plagioclase, anatase, ulvospinel, and maghemite were identified with laboratory Raman and XRD analyses (Table 2; Fig. 10; Fig. 9); a geochemical XY plot is shown in Figure 12d, showing tuffs and sandstones grouped by Fe_2O_3/TiO_2 ratios. It was apparent from the geological assessment of the field team that the tuffs were part of the emplacement history of the lacustrine sequence.; less than ten meters outside of the rover traverse (and outside of the traversable area) were larger outcrops of tuffs that were more easily identifiable than the "potatoes". Further evidence for the history of volcanics in the field are is the "popcorn" weathering texture of the lacustrine units. This texture is common in siltstones of the Painted Desert, Arizona, for example, where abundant ash fall mixed with lake deposits during their emplacement (Harris et al., 1997). Montmorillonite dominates the mineralogy of the lacustrine units, which is largely sourced from the ash fall deposits, having mixed with other very fine-grained materials during deposition.

Another major finding is that the lack of fresh outcrop surfaces also obscured the mineralogy. Although disseminated erosional material and ephemeral evaporitic lenses eroding out of the lacustrine units was identified as gypsum during the mission, it was found to be much more widespread during the post-mission field visit, particularly in the very shallow subsurface.

Abundant, well-crystallized cm-scale veins of gypsum were discovered several cm below the surfaces of siltstone units (e.g., Fig. 8c).

Raman, VIS-IR, and pXRD analysis also shows that both the sandstone and siltstone units comprises gypsum, clays, sulfates, and zeolites (Table 2; Figs. 5–10), which indicate post-emplacement diagenesis; sulfates (e.g., gypsum), Ca-phosphates (e.g., brushite), and Fe-oxyhydroxides (e.g., ferrihydrite) can be indicators of metabolic potential within the depositional and/or diagenetic environment (Mojzsis and Arrhenius, 1998; Lucas and Prévôt, 1984; Gramp et al., 2010). The greenish mudstones (Neils) were thought to have the best organic matter preservation potential, interpreted to have formed in a reducing environment near the channel floodplain-lacustrine interface (unit 3, Fig. 3). Dysoxic to anoxic conditions result from the exhaustion of free oxygen produced through the oxidation of organic matter in the isolated deep zone of a lake. The darker green coloration, geochemistry, and mineralogy led the team to interpret its emplacement in reduced depositional environment, and therefore this lithology was postulated as the best candidate for biosignature preservation. Purple-black bands of the red mudstones were ranked as the second highest priorities as dark purple colors often indicate high TOC and/or oxidized conditions. Preservation pathways for organic carbon are known in oxide and oxyhydroxide minerals, and the in-sim Science Team hypothesized that the cm-scale purple lenses may indicate past habitable environments, as dark coloration could potentially indicate an even more reducing environment than represented by the green shales. However, the lacustrine units failed to show higher TOC levels than the conglomerates and sandstones of the field site (Thyrmhiem and Hans, Table 3). This is unexpected, as generally, mudstones and siltstones, and particularly shales, have a much higher likelihood of having formed and preserved organic carbon, even with a substantial influx of volcanic ash sediments (Yuan et al., 2016). In fact, the level of TOC found in all site samples (at ≥0.03 wt %) was 100 times less than is considered organic-rich for sedimentary rock (Boggs, 2006). Potential explanations for the low TOC include: 1) the lacustrine units having a large component of volcanic ash and thus not as rich in bioavailable elements, 2) preservation of organic carbon may not have been favored through diagenesis, and/or 3) formation of organic carbon may not have initially been favorable. Preservation of TOC is highly dependent on the weathering state and general preservation of the lithologies (Petsch et al., 2000). Marynowski et al. (2011) showed that in addition to the effects of surficial weathering, paleoweathering processes, given oxidative paleoenvironmental conditions, may significantly decrease TOC. The mudstone samples were not "fresh" surfaces, as it was not possible for the rover to access below the hard popcorn-textured, weathered surface (50 mm was the maximum depth of MESR drill core); therefore, it was difficult to reasonably assess primary TOC or the effect of surficial weathering without deeper drilling.

The findings of TOC levels in the samples from the field site certainly does warrant further investigation as to the ways in which organic matter is preserved on Earth in environments analogous to those which will be pursued with the same exploration goals on Mars. It also further suggests that careful, thorough characterization of potential landing sites through remote science coupled with in-depth analogous studies are critical to understanding our capabilities for addressing the Mars exploration goals as set forth by the community through MEPAG. Given the scientific and technological risks and high cost of planetary robotic missions, there is great interest in analogous field studies, and in determining how well rover missions meet their goals; the latter was addressed by the closely-simulated CanMars in-sim mission. The field team provided an in-depth geologic assessment of a little-studied field area in Utah that serves as an important analogue to similar features on Mars ranked as high exploration potential for future missions. The regional geology as interpreted by the field team is provided in the following section.

5.3. Implications for the regional geology of south-central Utah

In addition to providing ground-truth data for the CanMars in-sim science results, the analyses presented in this paper provide a physiochemical, mineralogical, spectroscopic, and petrographic characterization of the field site with wider implications. Montmorillonite is the dominant mineralogy in the multi-colored lacustrine sequences, present as a product of diagenesis of lacustrine and silicic volcanic ash fall deposits, as described for the region by Demko et al. (2004). These deposits therefore serve as an excellent analogue to clay-rich regions on Mars, where aqueous activity may have altered extensive volcanic deposits in the ancient terrains; such ancient deposits are currently being considered for the ExoMars 2018 rover site and represent those in the chosen site for the Mars 2020 rover mission. This study furthermore gives geologic context to the formation and potential preservation of inverted paleochannel terrain on Mars present due to fluvial sedimentation and cementation (Tanaka and Kolb, 2001); the identification of sedimentary structures such as cross-bedding would confirm a fluvial emplacement. Cross-bedding is common in the paleochannel formations of this study, particularly in the conglomeratic capping unit. Furthermore, paleochannel formations were hypothesized prior to the analogue mission via areal imagery as the measured sinuosity was consistent with fluvially-capped paleochannel morphology (Williams et al., 2011). A schematic of inverted paleochannel formation is shown in Figure 14 and illustrates the basic geologic history of the field area of this study.

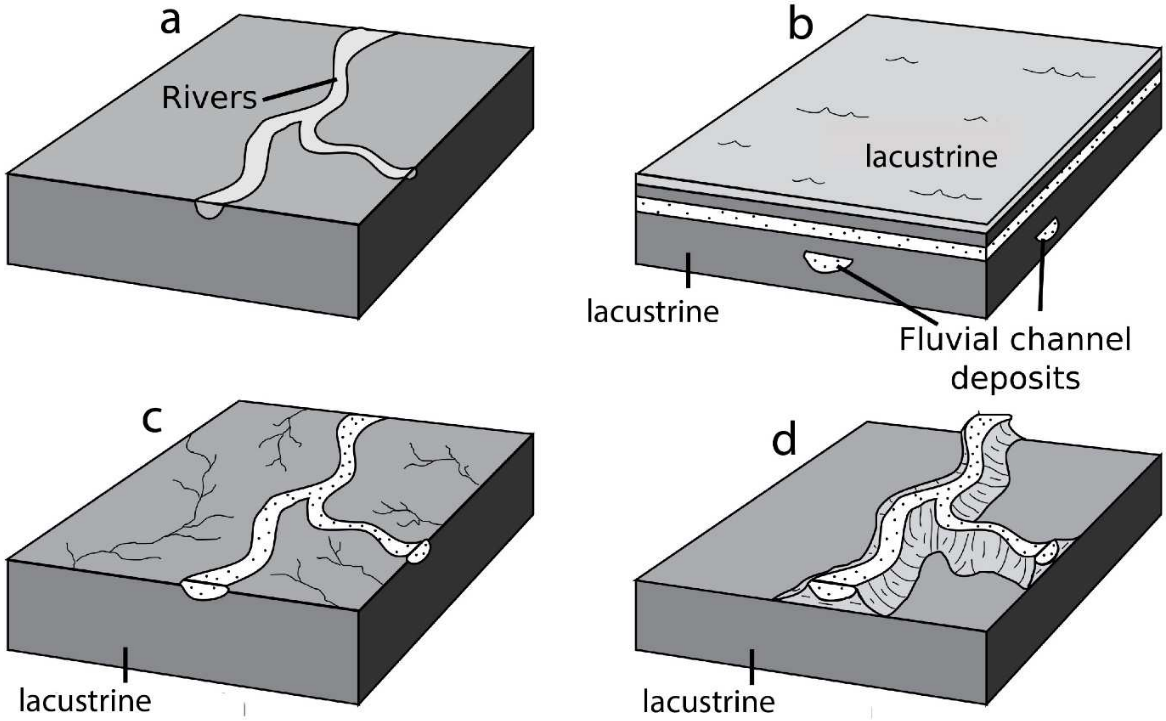

Figure 14. Step-wise illustration of paleochannel formation (after Williams et al., 2007). Alluvial floodplain environments are shown in (a), common during the Early Cretaceous. Intermittent fluvial and lacustrine systems dominate the depositional environments (b), where fluvial channels leave lenticular sandstone beds, surrounded by low-energy lacustrine sedimentation. Sediments are buried and subsequently exhumed (c) due to regional uplift, transitioning the setting from depositional to erosional. (d) Present-day inverted paleochannels are formed, where well-cemented fluvial channels act as a capping unit, preserving the highly friable and sometimes unconsolidated, very fine, soft sediments.

The floodplain depositional environment, with soft lacustrine/ash fall sediments surrounding a braided channel environment (e.g., Fig. 14a) is reflected in the bottom-most units (e.g., Hans, unit 7 and Alfhiem, unit 8), where multiple generations of sandstones represent a braided channel environment. The sandstones were deposited in a low-medium energy floodplain, reflected in the discontinuous run-out, laminar cross-beds, and the many sandstone outcrops in the basin showing the paleo-topography of the channel system. The multiple generations of sandstones are seen in the differences in mineralogy and cementation; earlier sandstones (unit 8, Fig. 3) have calcite cementation (Fig. 11c–d), and the later sandstones (unit 7, Fig. 3) have complete silica (quartz and chert) cementation (Fig. 11a–b), as do the conglomeratic sandstones. Cementation differences reflect the age, as different ground water chemistry was available during diagenesis, though there exists the potential for an overprinting of the original cementation due to diagenetic crystal growth and alteration post-cementation. The early cementation allowed for preservation of the sandstones through burial and erosion. A reducing environment was present at the channel floodplain-lacustrine interface, where the green siltstones (unit 3, Fig. 3) are present. As shown in Figure 14b, lacustrine and silicic ash fall sediments were emplaced, burying the floodplain deposits.

The abundance of gypsum within the lacustrine units indicates their emplacement in semi-arid environment, where fluctuating water tables often created evaporitic conditions at the surface. The latest generation of channels was a high-energy channel, creating sandstone and conglomerates with pebble-cobble-sized clasts (unit 1, Fig. 3; e.g., Thrymhiem). The two paleochannels in the field area had different paleo-flow directions (Fig. 4), indicative of a low-relief depositional setting. These well-cemented channels created the capping unit, protecting the underlying lithologies from erosion as regional uplift caused mass erosion of the sediments in the basin (e.g., Fig. 9d).

This work represents the first in-depth geologic study of the field area and provides an opportunity to detail paleochannel formation events which is of interest for future Mars rover exploration. This study has combined data from three sources to confirm the history of lacustrine and paleochannel formation in this region: (1) data acquired within the context of the CanMars analogue mission (e.g., remote sensing data and rover-derived images and scientific measurements); (2) data acquired out-of-simulation by the field validation team (e.g., field maps and additional samples and images); and (3) laboratory-based analysis of samples returned by both parties.

6. Conclusions

This study presents an in-depth geological assessment of the 2015 – 2016 CanMars analogue mission field site near Hanksville, Utah. The field site is a present-day erosional basin in an arid environment with preserved and exposed Late Jurassic lacustrine/tuff and fluvial paleochannels. During the Jurassic, aqueously mobilized carbonate-rich and siliceous sediments were emplaced via a low-moderate energy, discontinuous braided stream bed in the center of the basin, represented by lenticular sandstones with planar cross-beds and soft-sediment deformation. This was followed by a period of lower sediment influx, lower energy lacustrine systems, having substantial volcanic ash fall material intermixed. Meandering streams were then emplaced atop of the lacustrine/volcanic basin fill material, forming strongly silica-cemented sandstones and conglomerates with moderate sinuosity and multiple flow directions. As the uplift of the Colorado Plateau shifted the geologic regime of the region to an erosional environment, the meandering streams acted as a capping unit, protecting the highly friable underlying lithologies from erosion. This resulted in the inverted paleochannel topography now exposed at the field site, where multiple channel segments extend for ~ 100 m with well-defined, m-scale trough cross-beds. The inverted paleochannels of this region may be apt Mars analogues for the Martian wind-exhumed, inverted fluvial channels that may have also preserved widespread volcanic ash-fall and lacustrine deposits (e.g., Hynek, 2003; Fassett and Head, 2008). Analogue studies such as this are timely as near-future Mars landing sites containing inverted channels are also being considered as potential landing sites for ExoMars 2018 (e.g., Aram Dorsum; Balme et al., 2016) and Mars 2020 rovers (e.g., Melas Chasma; Davis et al., 2015).

This study furthermore details the out-of-sim operations of the field team operating in the CanMars mission which may be of interest to future analogue mission deployments. The field team collected duplicate samples as well as samples further afield of the CanMars in-sim rover-traversable bounds ("out-of-sim" samples), acting as a validation of the in-sim findings of a remote rover operations science mission (detailed by Caudill et al., 2019). While the instrumentation and operational strategies allowed the in-sim rover team to assess the geology by building a depositional model throughout the mission (Caudill et al., 2019; Pilles et al., 2019), there were many details of the geology and terrain that were missed due to factors including mobility, traversability, time constraints and the inherent difficulty in remotely assessing geologic context. Given the available rover instrument suite, drilling, and sampling capabilities, the detection of past life with the within the context of paleochannel and highly erosional lacustrine-tuff deposits proved difficult. The comparative efficiency and efficacy of the MESR rover and a human geologist is covered in Beaty et al. (2019).

Given the inherent rover handicaps, the instrument suite provided data appropriate for the in-sim team to assess geologic context and choose samples that were representative of the major, important lithologies of the site, allowing for an in-depth analysis of the site through the "returned" samples. However, the lack of TOC sampled in an environment that may have been initially favorable for its formation warrants further investigation with regard to lacustrine-tuff deposits, preservation potential of ancient life, and critically, the depths at which these materials are likely to be preserved and sampled. This also suggests that careful, thorough remote characterization of analogous sites on Mars which are potential landing sites is crucial; furthermore, continued in-depth field studies are also recommended to best understand the potential to address Mars exploration goals, including identifying past habitability, preservation, and presence of past life in specific environments.

7. Acknowledgments

We thank the CSA and the CanMars team for the dedication and long hours spent which made this mission a reality. Our international guests (from NASA, UKSA, DLR, and other institutions) aided us in making this a high-fidelity analogue mission and helped us make most of this opportunity for future MSR efforts. The CSA Mars Exploration Science Rover (MESR) used in this exercise was built by MDA Maxar. The analogue mission was carried out in partnership between the Canadian Space Agency and the Centre for Planetary Science and Exploration (CPSX) at the University of Western Ontario, as part of the NSERC CREATE project "Technologies and Techniques for Earth and Space Exploration" (create.uwo.ca). We would also like to acknowledge Hans van 't Woud of Blackshore and its partners, including European Space imaging and EuroMoonMars research for the use of the colour Quickbird-2 image that covers the

CanMars analogue mission site. KHW and MLT acknowledge the support of a grant from the National Aeronautics and Space Administration for work performed at the Jet Propulsion Laboratory, California Institute of Technology.

8. References

Antonenko, I., Osinski, G.R., Battler, M., Beauchamp, M., Cupelli, L., Chanou, A., Francis, R., Mader, M.M., Marion, C., McCullough, E., Pickersgill, A.E., Preston, L.J., Shankar, B., Unrau, T., et al., 2013, Issues of geologically-focused situational awareness in robotic planetary missions: Lessons from an analogue mission at Mistastin Lake impact structure, Labrador, Canada: Advances in Space Research, v. 52, p. 272–284, doi: 10.1016/j.asr.2012.11.024.

Balme, M., Grindrod, P., Sefton-Nash, E., Davis, J., Gupta, S., and Fawdon, P., 2016, Aram Dorsum, Candidate ExoMars Rover Landing Site: a Noachian Inverted Fluvial Channel System in Arabia Terra Mars: Geophysical Research Abstracts EGU General Assembly, v. 18, p. 2016–14030, doi: 10.1029/2002JE001891.

Beaty, D.W., Hipkin, V.J., Caudill, C.M., Hansen, R.F., Hausrath, E.M., Maggiori, C., McCoubrey, R., Parrish, J.C., Ralston, S.J. (2019) Geological Evaluation of the MSRAD Field Site by a Human Field Party: Implications for Rover-based Exploration Operations and for the Future Human Exploration of Mars. Planetary and Space Science, https://doi.org/10.1016/j.pss.2019.03.001

Beegle, L., Bhartia, R., White, M., Deflores, L., Abbey, W., Wu, Y.H., Cameron, B., Moore, J., Fries, M., Burton, A., Edgett, K.S., Ravine, M.A., Hug, W., Reid, R., et al., 2015, SHERLOC: Scanning habitable environments with Raman & luminescence for organics & chemicals, *in* IEEE Aerospace Conference Proceedings, v. 2015–June, doi: 10.1109/AERO.2015.7119105.

Bourassa, M., Osinski, G. R., Tornabene, L. L., Caudill, C., Christoffersen, P., Daly M., Godin, E., Pilles, E. A., and Ryan, C. 2019. TEMMI, a Three-dimensional Exploration Multispectral Microscope Imager for planetary-exploration missions. Planetary and Space Science 165:57–74.

Caudill, C.M., Pontefract, A., Osinski, G. R., Tornabene, L. L., Xie, T., Mittelholz, A., Poitras, J., Simpson, S., Svensson, M., Grau, A. G., Godin, E., Pilles, E., Francis, R., Williford, K., Tuite, M., Battler, M., Hipkin, V., Haltigin, T., and the 2015 & 2016 Science Team members (2019) CanMars Mission Science Results and Review of Optimization for Sample Selection for Mars Sample Return (MSR) based on Science Operations and Procedures. Planetary and Space Science, https://doi.org/10.1016/j.pss.2019.04.004.

Clark, R.N., Swayze, G.A., Wise, R., Livo, K.E., Hoefen, T.M., Kokaly, R.F., Sutley, S.J., Survey, U.S.G., and Title, S., 2007, USGS Digital Spectral Library splib06a: U.S. Geological Survey, p. Digital Data Series 231, http://speclab.cr.usgs.gov/spectral.lib06.

Clay Minerals Society (CMS), 2016, The Clay Minerals Society Glossary of Clay Science:, http://www.clays.org/ClayTermsApril2017.pdf.

Coates, A.J., Jaumann, R., Griffiths, A.D., Leff, C.E., Schmitz, N., Josset, J.-L., Paar, G., Gunn, M., Hauber, E., Cousins, C.R., Cross, R.E., Grindrod, P., Bridges, J.C., Balme, M., et al., 2017, The PanCam Instrument for the ExoMars Rover: Astrobiology, v. 17, p. 511–541, doi: 10.1089/ast.2016.1548.

Compton, J.S., 1991, Origin and diagenesis of clay minerals in the monterey formation, Santa Maria Basin Area, California: Clays and Clay Minerals, v. 39, p. 449–466, doi: 10.1346/CCMN.1991.0390501.

Craig, L.C., Holmes, Cl.N., Cadigan, R.A., Freeman, V.L., Mullens, T.E., and Weir, G.W., 1955, Stratigraphy of the Morrison and Related Formations, Colorado Plateau Region: A Preliminary Report: Geological Survey Bulletin, v. 1009, p. 125–168, https://pubs.usgs.gov/bul/1009e/report.pdf.

Van Daele, M., Moernaut, J., Silversmit, G., Schmidt, S., Fontijn, K., Heirman, K., Vandoorne, W., De Clercq, M., Van Acker, J., Wolff, C., Pino, M., Urrutia, R., Roberts, S.J., Vincze, L., et al., 2014, The 600 yr eruptive history of Villarrica Volcano (Chile) revealed by annually laminated lake sediments: Bulletin of the Geological Society of America, v. 126, p. 481–498, doi: 10.1130/B30798.1.

Das, S., Hendry, M.J., and Essilfie-Dughan, J., 2011, Transformation of two-line ferrihydrite to goethite and hematite as a function of pH and temperature: Environmental Science and Technology, v. 45, p. 268–275, doi: 10.1021/es101903y.

Davis, J., Grindrod, P., Williams, R., Gupta, S., and Balme, M., 2015, Stratigraphy Evidence of Episodic Fluvial Activity in the South Melas Chasma Basin, Valles Marineris, Mars, *in* Lunar and Planetary Science Conference, p. 1932.

Demko, T.M., Currie, B.S., and Nicoll, K.A., 2004, Regional paleoclimatic and stratigraphic implications of paleosols and fluvial/overbank architecture in the Morrison Formation

(Upper Jurassic), Western Interior, USA: Sedimentary Geology, v. 167, p. 115–135, doi: 10.1016/j.sedgeo.2004.01.003.

Derr, M.E., 1974, Sedimentary structure and depositional environment of paleochannels in the Jurassic Morrison Formation near Green River, Utah: Brigham Young University Geology Studies, v. 21, p. 3–39.

Eshelman, E., Daly, M.G., Slater, G., Dietrich, P., and Gravel, J.F., 2014, An ultraviolet Raman wavelength for the in-situ analysis of organic compounds relevant to astrobiology: Planetary and Space Science, doi: 10.1016/j.pss.2014.01.021.

Farr, T.G., 2004, Terrestrial analogs to Mars: The NRC community decadal report, *in* Planetary and Space Science, v. 52, p. 3–10, doi: 10.1016/j.pss.2003.08.004.

Fassett, C.I., and Gouge, T.A., 2017, Hydrological Modeling of the Jezero Crater Outlet-Forming Flood, *in* Lunar and Planetary Science Conference, p. 2037.

Fassett, C.I., and Head, J.W., 2005, Fluvial sedimentary deposits on Mars: Ancient deltas in a crater lake in the Nili Fossae region: Geophysical Research Letters, v. 32, p. 1–5, doi: 10.1029/2005GL023456.

Fassett, C.I., and Head, J.W., 2008, Valley network-fed, open-basin lakes on Mars: Distribution and implications for Noachian surface and subsurface hydrology: Icarus, v. 198, p. 37–56, doi: 10.1016/j.icarus.2008.06.016.

Fortin, D., Leppard, G.G., and Tessier, A., 1993, Characteristics of lacustrine diagenetic iron oxyhydroxides: Geochimica et Cosmochimica Acta, v. 57, p. 4391–4404, doi: 10.1016/0016-7037(93)90490-N.

Foster, J.R., 2003, Paleoecological analysis of the vertebrate fauna of the Morrison Formation (Upper Jurassic), Rocky Mountain Region, U.S.A.: Albuquerque, NM, New Mexico Museum of Natural Hisstory and Science, 1-70 p.

Goudge, T.A., Mohrig, D., Cardenas, B.T., Hughes, C.M., and Fassett, C.I., 2018, Stratigraphy and paleohydrology of delta channel deposits, Jezero crater, Mars: Icarus, v. 301, p. 58–75, doi: 10.1016/j.icarus.2017.09.034.

Gramp, J.P., Bigham, J.M., Jones, F.S., and Tuovinen, O.H., 2010, Formation of Fe-sulfides in cultures of sulfate-reducing bacteria: Journal of Hazardous Materials, v. 175, p. 1062–1067, doi: 10.1016/j.jhazmat.2009.10.119.

Grotzinger, J.P., Gupta, S., Malin, M.C., Rubin, D.M., Schieber, J., Siebach, K., Sumner, D.Y., Stack, K.M., Vasavada, A.R., Calef, F., Edgar, L., Fischer, W.F., Grant, J.A., Griffes, J., et al., 2015, Deposition, exhumation, and paleoclimate of an ancient lake deposit, Gale crater, Mars: Science, v. 350, http://www.sciencemag.org/cgi/doi/10.1126/science.aac7575.

Harms, J.C., 1979, Primary Sedimentary Structures: Annual Review of Earth and Planetary Sciences, v. 7, p. 227–248, doi: 10.1146/annurev.ea.07.050179.001303.

Harris, A.G., Tuttle, E., and Tuttle, S.D., 1997, Geology of National Parks: Kendall/Hunt Publishing Company, 102-112 p.

Hintze, L.H., and Kowallis, B.J., 2009, The Geology History of Utah: Brigham Young University Geology Studies Special Publication 9, Department of Geology, Brigham Young University, Provo, Utah,.

Hynek, B.M., 2003, Explosive volcanism in the Tharsis region: Global evidence in the Martian geologic record: Journal of Geophysical Research, v. 108, p. 5111, doi: 10.1029/2003JE002062.

Izawa, M.R.M., Applin, D.M., Norman, L., and Cloutis, E.A., 2014, Reflectance spectroscopy (350-2500 nm) of solid-state polycyclic aromatic hydrocarbons (PAHs): Icarus, doi: 10.1016/j.icarus.2014.04.033.

Lafuente, B., Downs, R.T., Yang, H., and Stone, N., 2015, The power of databases: the RRUFF project, *in* Danisi, T.A. and R.M. ed., Highlights in Mineralogical Crystallography, Berlin, Germany, W. De Gruyter.

Lucas, J., and Prévôt, L., 1984, Synthèse de l'apatite par voie bactérienne à partir de matière organique phosphatée et de divers carbonates de calcium dans des eaux douce et marine naturelles: Chemical Geology, v. 42, p. 101–118, doi: 10.1016/0009-2541(84)90008-1.

Marynowski, L., Kurkiewicz, S., Rakociński, M., and Simoneit, B.R.T., 2011, Effects of weathering on organic matter: I. Changes in molecular composition of extractable organic compounds caused by paleoweathering of a Lower Carboniferous (Tournaisian) marine black shale: Chemical Geology, doi: 10.1016/j.chemgeo.2011.04.001.

Malin, M.C., and Edgett, K.S., 2003, Evidence for Persistent Flow and Aqueous Sedimentation on Early Mars: Science, v. 302, p. 1931–1934, doi: 10.1126/science.1090544.

McKeown, N.K., Bishop, J.L., Cuadros, J., Hillier, S., Amador, E., Makarewicz, H.D., Parente, M., and Silver, E.A., 2011, Interpretation of reflectance spectra of clay mineral-silica mixtures:Implications for Martian clay mineralogy at Mawrth Vallis: Clays and Clay Minerals, v. 59, p. 400–415, doi: 10.1346/CCMN.2011.0590404.

McLennan, S.M., Sephton, M.A., Allen, C., Allwood, A.C., Barbieri, R., Beaty, D.W., Boston, P., Carr, M., Grady, M., Grant, J., Heber, V.S., Herd, C.D.K., Hofmann, B., King, P., et al., 2012, Planning for Mars Returned Sample Science: Final Report of the MSR End-to-End International Science Analysis Group (E2E-iSAG): Astrobiology, v. 12, p. 175–230, doi: 10.1089/ast.2011.0805.

Mojzsis, S.J., and Arrhenius, G., 1998, Phosphates and carbon on Mars: Exobiological implications and sample return considerations: Journal of Geophysical Research-Planets, v. 103, p. 28495–28511, doi: 10.1029/98je02141.

NASA, 2013, Vision and Voyages for Planetary Science in the Decade 2013-2022: Washington, D.C., THE NATIONAL ACADEMIES PRESS.

Osinski, G.R., Battler, M., Caudill, C.M., Francis, R., Haltigin, T., Hipkin, V.J., Kerrigan, M., Pilles, E.A., Pontefract, A., Tornabene, L.L., Allard, P., Bakambu, J.N., Balachandran, K., Beaty, D.W., et al., 2019, The CanMars Mars Sample Return analogue mission: Planetary and Space Science, doi: 10.1016/j.pss.2018.07.011.

Pain, C.F., Clarke, J.D.A., and Thomas, M., 2007, Inversion of relief on Mars: Icarus, v. 190, p. 478–491, doi: 10.1016/j.icarus.2007.03.017.

Petsch, S.T., Berner, R.A., and Eglinton, T.I., 2000, A field study of the chemical weathering of ancient sedimentary organic matter, *in* Organic Geochemistry, v. 31, p. 475–487, doi: 10.1016/S0146-6380(00)00014-0.

Pilles, E.A., Cross, M., Caudill, C.M., Francis, R., Osinski, G.R., Newman, J., Battler, M., Bourassa, M., Haltigin, T., Hipkin, V., Kerrigan, M., McLennan, S., Silber, E.A., and Williford, K., 2019, Exploring new models for improving planetary rover operations efficiency through the 2016 CanMars Mars Sample Return (MSR) analogue deployment: Planetary and Space Science, doi: 10.1016/j.pss.2018.10.001.

Rice, M.S., Bell, J.F.I., Gupta, S., Warner, N.H., and Anderson, R.B., 2013, A detailed geologic characterization of Eberswalde crater , Mars: MARS, The International Journal of Mars Science and Exploration, v. 8, p. 15–57, doi: 10.1555/mars.2013.0002.

Ryan, C.H., Haid, T.M., Osinski, G.R., and Tornabene, L.L., 2016, 2015 CanMars MSR Analogue Mission: The Utilization of the Three-Dimensional Exploration Multispectral Microscopic Imager (TEMMI) for In Situ Analysis: 47th Lunar and Planetary Science Conference, p. Abstract #1991, http://www.lpi.usra.edu/meetings/lpsc2016/pdf/1991.pdf.

Speight, J.G., 2017, Sources and Types of Inorganic Pollutants, *in* Environmental Inorganic Chemistry for Engineers, Butterworth-Heinemann, p. 231–282.

Stedwell, C.N., and Polfer, N.C., 2013, Spectroscopy and the Electromagnetic Spectrum, *in* Polfer, N.C., Dugourd, P. ed., Laser photodissociation and spectroscopy of mass-separated biomolecular ions, Springer, p. 1–20.

Summons, R.E., Amend, J.P., Bish, D., Buick, R., Cody, G.D., Des Marais, D.J., Dromart, G., Eigenbrode, J.L., Knoll, A.H., and Sumner, D.Y., 2011, Preservation of Martian Organic and Environmental Records: Final Report of the Mars Biosignature Working Group: Astrobiology, v. 11, p. 157–181, doi: 10.1089/ast.2010.0506.

Tanaka, K.L., and Kolb, E.J., 2001, Geologic history of the polar regions of Mars based on Mars Global survey data. I. Noachian and Hesperian Periods: Icarus, v. 154, p. 3–21, doi: 10.1006/icar.2001.6675.

Wiens, R.C., Maurice, S., and Perez, F.R., 2017, The SuperCam remote sensing instrument suite for the Mars 2020 rover: a preview: Spectroscopy, v. 32, p. 50.

Williams, R.M.E., Chidsey, T.C., J., and Eby, D.E., 2007, Exhumed paleochannels in central Utah—Analogs for raised curvilinear features on Mars, *in* Willis, G.C., Hylland, M.D., Clark, D.L., and Chidsey, T.C., J. eds., Central Utah—Diverse Geology of a Dynamic Landscape, Utah Geological Association Publication, p. 220–235.

Williams, R.M.E., Irwin, R.P.I., Zimbelman, J.R., Chidsey, T.C., J., and Eby, D.E., 2011, Field guide to exhumed paleochannels near Green River,Utah: Terrestrial analogs for sinuous ridges on Mars, *in* Garry, W.B. and Bleacher, J.E. eds., Analogs for Planetary Exploration: Geological Society of America Special Paper 483, The Geological Society of America, p. 483–505.

Yuan, W., Liu, G., Luo, W., and Li, C., 2016, The Influence of Volcanic Ash Sediments on the Formation of Lacustrine Organic-Rich Shale in Ordos Basin, Central China, *in* AAPG Annual Convention and Exhibition, Calgary, Alberta, Canada, p. 90259.

Appendix 1. All “in-sim” (CSA) and “out-of-sim” (CST) samples, with notes (with relevant target names) and descriptions. See Figures 2 and 3 for sample location information.

ID	Latitude/ Easting	Longitude/ Northing	Rock Type	Notes	Hand Sample Description
CSA-001	38.418442	-110.785125	Sandstone	Outcrop Alfheim; first in-sim core acquired in 2015; bottom-most sandstone unit	White rock with a dark brown weathering surface. Carbonate-cemented arkosic sandstone. Large (~ 10 cm-wide)

					concretions common. Has a medium-lower grain size and is well-sorted. Potential micro-fossils are present.
CSA-002	38.417711	-110.784974	Clastic sandstone/ conglomeratic sandstone	Target Idi on outcrop Thrymhiem; boulder fall from conglomeratic unit capping inverted channel. Second 2015 in-sim core.	Polymict conglomerate with a pinkish-white (mostly) clast-supported matrix. Clasts range in size from 1 mm to 1.5 cm, are sub- to well-rounded, and are likely primarily quartz in composition, with chert, feldspars, and some lithics. The matrix also appears primarily quartz in composition and is fine-lower to medium-lower in grain size.
CSA-003	38.417495	-110.785038	vfg white crystalline lens	Target Gimli at base of Jotenheim (inverted channel). Third 2015 in-sim sample.	White crystalline lens at base of Jotenheim (inverted channel); powder sample
CSA-004	38.41575	-110.78446	Regolith/soil sample	Target Fimbulvetr at Fenrir, loose soil sample; red/tan partially desiccated material found throughout floor of region; Fourth 2015 in-sim sample.	Regolith/soil sample; red-tan vfg basin floor material
CSA-005 / CST-2016-005	38.415742	-110.784467	Sandstone	Target Hans, first 2016 in-sim sample. Quartz arenite with brown weathering exhibits circular and other sedimentary structures with cm-scale thick laminations, ripple marks on exposed surfaces, and pits potentially formed by ebb currents in active river systems. Underlying rock is a poorly consolidated white quartz rich sandstone-siltstone with no sedimentary features.	Polymict, clast-dominated conglomerate with a white coloured matrix. Clasts are sub- to well-rounded, range in size from 1 mm to 1 cm, and appear mostly quartz in composition. Matrix is fine-upper* in grain size.
CSA-006 / CST-2016-025	38.416031	-110.784894	Mudstone	Target Astrid, second 2016 in-sim sample. Purplish-red very fine-grained mudstone.	Highly oxidized, dark-red argillaceous mudstone. Has a very fine-lower to fine-upper grain size and appears well-sorted. Small black grains visible.
CSA-007 / CST-2016-056	38.416007	-110.785178	Mudstone	Target Scyld, third 2016 in-sim sample. White/green mudstone, sampling popcorn-textured erosional face. At nearby CST-2016-048, gypsum and orange alteration is found with potential pyrite.	Greenish-grey argillaceous mudstone (reddish-brown weathering surface) displaying fissility. Has a very fine-upper grain size and appears well-sorted.
CSA-008 / CST-2016-028A	38.416007	-110.785123	Mudstone	Target Niels, fourth 2016 in-sim sample. Green mudstone, popcorn-textured erosional face. Gypsumiferous with orange alteration. Ranked highest for potential for TOC.	Greenish-grey argillaceous mudstone (orange-brown weathering surface) displaying fissility. Very fine grain size and appears well-sorted.
CST-2015-001	38.418442	-110.785125	Sandstone	Sample near Alfheim.	White rock with a dark brown weathering surface. Carbonate-cemented arkosic sandstone. Large (~ 10 cm-wide) concretions common. Has a medium-lower grain size and is well-sorted. Potential micro-fossils are present.
CST-2015-002	38.418442	-110.785125	Sandstone	Sample of Sif, near sample Alfheim and same outcrop.	White rock with a dark brown weathering surface. Carbonate-cemented arkosic sandstone. Large (~ 10 cm-wide) concretions common. Has a medium-lower grain size and is well-sorted. Potential micro-fossils are present.
CST-2015-003	38.418442	-110.785125	Powder soil sample	Pinkish, mixed soil sample below Alfheim outcrop.	Pinkish unconsolidated vfg sediment.
CST-			Unconsolidated	Kristoff sample, unconsolidated	Pinkish unconsolidated vfg sediment. size.

2015-015			soil sample	sample from basin floor and a past or currently active stream bed.	
CST-2015-016			Unconsolidated soil sample	Kristoff, second sample, unconsolidated sample from basin floor and a past or currently active stream bed.	Pinkish unconsolidated vfg sediment.
CST-2015-019	38.417495	-110.785038	Mudstone	Himinbjord sample, which is the red layer of Jotenheim.	Red, apparently oxidized, argillaceous mudstone displaying fissility; vfg and well-sorted.
CST-2015-023	38.417495	-110.785038	Unconsolidated soil sample	Modgud powdered sample, near Gimli (CSA-003). White, crystalline and Mg-rich material on basin floor and bottom of Jotenheim.	White crystalline lens at base of Jotenheim (inverted channel); powder sample
CST-2015-024	38.417495	-110.785038	Unconsolidated soil sample	Modgud, second powdered sample, near Gimli (CSA-003). White, crystalline and Mg-rich material on basin floor and bottom of Jotenheim.	White crystalline lens at base of Jotenheim (inverted channel); powder sample
CST-2015-025	38.41575	-110.78446	Unconsolidated soil sample	Gjoll sample, near Kristoff; possibly fresh, small stream bed	Pinkish unconsolidated vfg sediment.
CST-2015-026	38.417495	-110.785038	Mudstone	White mudstone sample near Himinbjord sample in Jotenheim.	White argillaceous mudstone displaying fissility; vfg and well-sorted.
CST-2016-001	38.415762	-110.783557	Sandstone	Circular pits on the surface of Quartz arenite. Erosion features presumably created by water environments.	White and pink, laminated sandstone with a brown weathering surface. Has a medium-lower to medium-upper grain size.
CST-2016-002	38.415775	-110.783568	Sandstone	Non-pitted Quartz arenite. Red colouring is extensive in the thin beds, weathering didn't solely affect the surface.	Coarse, pink and white coloured sandstone with a light brown weathering surface. Has a medium-lower to coarse-lower grain size and appears poorly-sorted. Very few, scattered, rounded clasts up to 5 mm in size.
CST-2016-003	38.415749	-110.783976	Sandstone	Fine grained, Quartz rich sandstone with 1mm empty cavities. Black minerals, <1mm, comprise 5% of the sandstone. The minerals may actually be weathering which was incorporated into the sandstone whilst it was unconsolidated.	Pink and white coloured sandstone with a brown weathering surface. Has a medium-lower to medium-upper grain size and appears moderately-sorted.
CST-2016-004	38.415888	-110.784346	Tuff	Clast representing the outcrop prior to weathering sits along the contact between the white and red horizon. Underlying the white and red layers is a mixture of both white and red sediments (Quartz and iron oxides). Quartz rich, fine-grained, present in pillow shapes. Difficult to break using rock hammer, and peels off as layers instead of large clasts.	White with a minor red weathering pattern. Has a fine-medium grain size and appears well-sorted.
CST-2016-006	38.417051	-110.7866385	Tuff	Near the conglomerate from SW side of Jotenheim showing deep cavities (perhaps dissolution of carbonates or wethering out of clasts)	Pink, laminated, with interbeds of a more weather resistant, quartz-dominated composition. Has a fine-lower to medium-lower grain size and appears moderately-sorted.
CST-2016-007	38.417034	-110.7871082	Tuff	Piece of fine ground sandstone (loose rock; not in original place)	Strongly laminated, pinkish-white with a brown weathering surface. Has a medium-upper grain size and appears well-sorted.
CST-2016-008	38.41744	-110.7870726	Tuff	A rounded pieced of medium grained sandstone formed from concentric layers. This sample was taken off like an onion peel	Coarse, white with a reddish-brown weathering surface. Has a medium-upper to coarse-lower grain size and appears moderately- to poorly-sorted. Small black and red grains scattered throughout the

					sample.
CST-2016-009	38.418464	-110.7851222	Tuff	Moderately sorted medum grained sandstone of Alfheim ridge	White with a light brown weathering surface. Has a fine-upper grain size and appears well-sorted. Small black and red grains scattered throughout the sample.
CST-2016-010	38.417607	-110.7850331	Hematite-stained tuff	Sample is 4 m East of Thyrnheim; well sorted blocky sandstone. Sample was collected in place.	White with a blotchy pink pattern (from hematite weathering?). Has a fine-upper to medium-lower grain size and appears moderately-sorted. Coarser (1 mm), reddish brown grains sorted throughout the sample.
CST-2016-011	38.416546	-110.7862848	Tuff	Tuff from opposite side of Jotenheim (Hel); rounded elongate sample	Very hard, white rock with a very prominent, dark brown weathering surface. Appears primarily quartz in composition with minor amounts of brown red and black coloured grains of the same size. Has a medium-lower grain size and appears moderately-sorted.
CST-2016-012	38.418102	-110.7843672	Tuff	Fine grained black rock found East of Hel. Rock was not in place but was collected as it does not conform to any observed lithologies seen.	Pinkish-white sandstone with a light brown weathering surface. Has a fine-upper to medium-lower grain size and appears well-sorted.
CST-2016-013	38.417923	-110.7851238	Conglomerate	Small seam of exposed grey rock between Valhalla Hills and Jotenheim.	Clast-dominated conglomerate with a pinkish matrix. Clasts are sub- to well-rounded and 3 mm to 1.5 cm in size. Matrix is medium-lower to medium-upper in grain size, and is likely quartz- and feldspar-dominated.
CST-2016-014	38.417641	-110.7838989	Sandstone	Conglomerate from North tip of Valhalla Hills	White sandstone with a prominent brown weathered surface. Has a fine-upper to medium-lower grain size and appears well-sorted. Likely, primarily quartz in composition.
CST-2016-015	38.417495	-110.785038	Sandstone	North Face of Jotenheim. Unit 1 in stratigraphy, light cream coloured, laminated, fine sandstone. Pre sample	White with a black weathered surface. Has a fine-lower to medium-lower grain size and appears well-sorted.
CST-2016-016	38.417445	-110.785062	Hematite-stained tuff	Outcrop ~10m up Jotenheim of white bulbous rock	White with a blotchy pink pattern (from hematite weathering?). Has a fine-lower to medium-lower grain size and appears well-sorted.
CST-2016-017	38.41739	-110.785045	Mudstone	Unit 5 in start col. Umber coloured, fissile mudstone.	Dark red, oxidized, argillaceous mudstone displaying fissility. Has a very fine-lower to very fine-upper grain size and appears well-sorted.
CST-2016-018	38.417327	-110.785039	Arkosic arenite	Unit 7 in strat col. Cross bedded fine and med grain sandstone	Pink, arkosic arenite. Has a medium-lower grain size and appears moderately- to well-sorted.
CST-2016-019	38.417207	-110.785179	Mudstone	Purple fissile mudstone outcrop unit 11 on strat column	
CST-2016-020	38.416225	-110.784625	Mudstone	Green outcrop of sandstone material nears the Hans and Ingrid exposure.	Green argillaceous mudstone with no fissility. Has a very fine-lower grain size and appears well-sorted. Sporadic, brown, mm to 1 cm scale possible carbonate grains within the mudstone.
CST-2016-021	38.417244	-110.785258	Conglomerate	Coarse grained sandstone cap rock material at Jotenheim.	White, matrix-dominated conglomerate. Clasts are sub- to well-rounded, are around 5 mm in size, and appear quartz-dominated. Matrix is medium-lower to medium-upper in grain size and is also

					likely quartz-dominated.
CST-2016-022	Unknown	Unknown	Hematite-stained tuff	Tuff, location unknown	White with a blotchy pink pattern (from hematite weathering?). Has a fine-upper to medium-lower grain size and appears moderately sorted. Coarser (1 mm), reddish brown grains sorted throughout the sample.
CST-2016-023	Unknown	Unknown	Arkosic Arenite		Pink, arkosic arenite. Has a medium-lower grain size and appears moderately- to well-sorted. Some coarser, 1-2 mm, weather-resistant quartz-rich clasts sorted throughout the sample.
CST-2016-024	38.415941	-110.785134	Mudstone	Next to 28A, horizontally in line. Purple, dark, cms long gypsum plates	Highly oxidized, dark red mudstone. Has a very fine-upper grain size and appears well sorted. Some scattered, lighter colour grains with dark, weathering/alteration haloes around them.
CST-2016-026	38.417711	-110.784974	Conglomerate	Clearly interceded with coarse and fine-grained layers. Sample with Thrymhiem (CSA-002) drill hole. Contains many small, rounded pebbles. Quartz- rich with some feldspar and a few lithic bright green pebbles. Coarse grained, silica-rich matrix, clast-supported.	Polymict conglomerate with a pinkish-white matrix. Clasts range in size from 1 mm to 1.5 cm, are sub- to well-rounded, and are likely primarily quartz in composition. The matrix also appears primarily quartz in composition and is fine-lower to medium-lower in grain size.
CST-2016-027	38.418442	-110.785125	Sandstone	Sample near Alfheim (CSA-001). Primary or secondary carbonate cement. More brittle than any of the sandstones.	White sandstone (brownish-red weathering surface) with very few scattered ~3 mm sized clasts, which are quartz-rich. Has a fine-upper to medium-lower grain size and appears moderately- to poorly-sorted.
CST-2016-028	Unknown	Unknown	Hematite-stained tuff		Coarse, white rock with a red weathering pattern. Has a medium-lower to coarse-lower grain size and appears moderately- to poorly-sorted. Pink (K-spar?) and black (biotite?) grains visible, primarily quartz.
CST-2016-029	38.416006	-110.784912	Mudstone	Green coherent mudstone/shale top of red	Greenish-grey, weakly consolidated sediment. Has a fine-lower grain size and appears well-sorted.
CST-2016-030	38.416334	-110.784589	Arkosic arenite	Target Hans, representative of CSA-005. Endoliths present below crust tiny green layer. Brown – dark brown weathered surface, with layers that easily chip off. Quartz arenite.	Pinkish-orange arkosic arenite displaying little fissility. Has a fine-lower to fine-upper grain size and appears well-sorted.
CST-2016-031	38.415988	-110.786244	Hematite-stained tuff	In second red clay layer. Half metre above tuff 2 Represents lower part of tuff3	White with a blotchy pink pattern (from hematite weathering?). Has a fine-upper to medium-lower grain size and appears moderately-sorted. Small black grains visible are likely biotite.
CST-2016-032	38.416011	-110.785017	Mudstone	Green finely laminated but grains visible. Outcrop of green in situ, finely laminated.. Grains are discernible so it is an isolated patch more like Gorm than the green shales	Greenish-grey argillaceous mudstone (reddish-brown weathering surface) displaying fissility. Has a very fine-upper grain size and appears well-sorted.
CST-2016-033	38.416009	-110.785078	Unconsolidated	gyspum viens/flakes and sulfides in red unit; transect just above Niels; dark red/black, organic-rich red unit in transect above Niels. Gavin022: red layer, bottom of transect	(No proper hand sample). Dark-red coloured unconsolidated sediment, with some flakes representing an argillaceous mudstone.

CST-2016-034	38.416003	-110.784888	Mudstone	Green laminated, below target Birger.	Greenish-grey argillaceous mudstone (brown weathering surface) displaying fissility. Has a very fine-lower to fine-upper grain size and appears well-sorted. Coarser (1 mm), reddish brown grains sorted throughout the sample.
CST-2016-035	38.415569	-110.786295	Mudstone		Dark red, oxidized, argillaceous mudstone displaying fissility. Has a very fine-lower to very fine-upper grain size and appears well-sorted. Contains liner-shaped trace fossils.
CST-2016-036	38.415991	-110.785836	Mudstone	Completely in white clay. Trace fossils are below. Rounded dimples in surface.	Dark red, oxidized, argillaceous mudstone displaying fissility. Has a very fine-lower to very fine-upper grain size and appears well-sorted. Contains liner-shaped trace fossils.
CST-2016-037	38.416161	-110.784567	Mudstone	green mudstone unit, out of sim range	Green argillaceous mudstone, displaying minor fissility. Has a very fine-lower grain size and appears well-sorted. Abundant, 1-2 cm sized, white, linear-shaped skeletal grains (tabulate corals?).
CST-2016-038	38.416307	-110.784583	Unconsolidated	Fine grained material between the caprock sandstones on top of the Hans outcrop and the sandstone that was sampled as Hans during the mission. Sampled as part of the suite of samples from the Hans area.	White, mostly unconsolidated sediment. Appears to have a fine-upper grain size.
CST-2016-039	38.416301	-110.784602	Arkosic arenite	K feldspar rich sandstone on top of the Hans outcrop. Pink panther. Pinker than Hans. More feldspars. Same grain size. Weathers to a dark brown. Also has endoliths. Pink stuff was always above our reach. Sampled as part of the suite of samples from the Hans area.	Pink arkosic arenite with a dark brown weathering surface. Has a fine-upper to medium-lower grain size and appears well-sorted. Small black grains visible are likely biotite.
CST-2016-040	38.416243	-110.784465	Siltstone	Green all the way through. Not a coating. Same med grain size as Hans. No layering. Very brittle easily breaks. Small Quartz and reddish coasts. Some blacker coating visible on top. Sampled as part of the suite of samples from the Hans area.	Green argillaceous mudstone with no fissility. Has a very fine-lower grain size and appears well-sorted. Sporadic, brown, mm to 1 cm scale possible carbonate grains within the mudstone.
CST-2016-041	38.416177	-110.786096	Hematite-stained tuff	Erosion pattern of rounded small indentations, light toned, white-beige-tan colour. Above red unit and below the white unit (at Ragnarok).	White with a blotchy pink pattern (from hematite weathering?). Has a fine-upper to medium-lower grain size and appears moderately-sorted. Coarser (1 mm), reddish brown grains sorted throughout the sample.
CST-2016-042	38.415569	-110.786295	Tuff	At the contact between the white-grey unit and red unit. Surrounded by popcorn-textured siltstones.	White with a blotchy pink pattern (from hematite weathering?). May be a quartz arenite. Has a fine-lower to fine-upper grain size and appears well-sorted.
CST-2016-043	38.418683	-110.784504	Sandstone	Sample of sandstone near Alfheim; carbonate-cemented sandstone. Collected ~15m from Alfheim in the direction away from Jotunheim. ~10 to 15 cm-wide concretions.	White rock with a dark brown weathering surface. Large (~ 10 cm-wide) concretions common. Has a medium-lower grain size and is well-sorted. Potential micro-fossils are present.

CST-2016-044	Unknown	Unknown	Conglomerate		Polymict, clast-dominated conglomerate with a white coloured matrix. Clasts are sub- to well-rounded, range in size from 1 mm to 1 cm, and appear mostly quartz in composition. Matrix is fine-upper to medium-lower in grain size.
CST-2016-045	38.416253	-110.784451	Sandstone	Sandstone with desert varnish. Dark black fine grained coating. Samples not in situ. Just boulders. Sampled as part of the suite of samples from the Hans area.	Very hard, white sandstone (or quartz arenite), with a very prominent, dark brown weathering surface. Appears primarily quartz in composition with minor amounts of brown red and black coloured grains of the same size. Has a medium-lower grain size and appears moderately-sorted.
CST-2016-046	38.417346	-110.784768	Mudstone	Contact at Astrid between very fine-grained largely unconsolidated red and green mudstone. Top layer is crispy, popcorn-textured, and locally white and bleached but underneath bleaching it is mostly green. Erosional material covers very finely-laminated shales.	Weakly consolidated greenish-grey and red argillaceous mudstone. Has a very fine-lower to fine-lower grain size and appears well-sorted.
CST-2016-047	38.416018	-110.78619	Hematite-stained tuff	Within second red clay layer. Half metre above tuff 2	White with a blotchy pink pattern (from hematite weathering?). Has a fine-upper to medium-lower grain size and appears moderately-sorted. Coarser (1 mm), reddish brown grains sorted throughout the sample.
CST-2016-048	38.416007	-110.785123	Mudstone	Whitish-greenish popcorn-textured unit with yellow alteration with well-formed gypsum crystals present several cm below surface. Representative of Scyld (CSA-007).	White-greenish argillaceous mudstone displaying fissility. Has a very fine-upper grain size and appears well-sorted.
CST-2016-049	38.415838	-110.78572	Hematite-stained tuff	Tuff layer, ~20cm thick, rounded gridlock pattern on top. About 2.5m above Tuff 3. Completely within the white unit.	White tuff with a brown weathered surface. Has a fine-lower to fine-upper grain size and appears well-sorted.
CST-2016-050	38.416021	-110.784983	Siltstone – Sandstone	Green laminated, below Biger. In situ.	White sandstone with a light brown weathering surface. Has a fine-upper to medium lower grain size and appears well-sorted. Small black and red grains scattered throughout the sample.
CST-2016-051	38.415941	-110.785134	Mudstone	Next to 28A, horizontally in line. Purple, dark, cms long gypsum plates	Dark red, oxidized, argillaceous mudstone displaying fissility. Has a very fine-lower to very fine-upper grain size and appears well-sorted.
CST-2016-052	38.415948	-110.784708	Siltstone	Green siltone, in situ.	Weakly consolidated, green and red siltstone. Has a very fine-upper to fine-lower grain size and appears well-sorted.
CST-2016-053	38.416221	-110.786099	Tuff	Tuffaceous white deposit near South face of Jotenheim	Pink and white, concentric-shaped sandstone. Has a has a fine-upper to medium-lower grain size and appears well-sorted.
CST-2016-054	38.41667	-110.788308	Siltstone		Greenish grey and red siltstone in a concentric shape with minor fissility. Has a very fine-upper to fine-upper grain size and appears well sorted.
CST-2016-055	38.417207	-110.785179	Mudstone	Purple fissile mudstone outcrop unit 11 on strat column	Dark red, oxidized, argillaceous mudstone displaying fissility. Has a very fine-lower to very fine-upper grain size and appears well-sorted.

CST-2016-057	38.416129	-110.7850375	Sandstone	potential organic-rich sandstone - glauconite (green, not black)	Powder from hand sample is white in colour, quartz-rich.
CST-2016-058	38.416009	-110.785086	Unconsolidated / Mudstone	Disturbed the surfaces of green-ish mudstone/shales; representative of sample ranked highest for organic and biosignature preservation (Niels)	No proper hand sample of unconsolidated sediment; appears to be from a vfg argillaceous mudstone with orange alteration of the popcorn-textured crust.
CST-2016-059	38.416005	-110.784888	Sandstone	Pinkish sandstone	Weakly consolidated, white sandstone with a light brown weathering surface. Has a fine-upper to medium-lower grain size and appears well-sorted. Small black and red grains scattered throughout the sample.
CST-2016-060	38.416011	-110.785017	Shaley Mudstone	Green shaley mudstone, small outcrop, finely laminated, and just missed by the rover team.	Greenish-grey argillaceous mudstone displaying fissility. Has a fine-lower grain size and appears well-sorted.
CST-2016-061	38.415991	-110.785836	Hematite-stained tuff	Completely within the white clay-rich unit. Trace fossils are below. Rounded dimples in surface.	White with a blotchy pink pattern (from hematite weathering?). Has a fine-lower grain size and appears well-sorted.
CST-2016-062	38.416009	-110.785078	Siltstone	Red layer, bottom of transit.	Weakly consolidated, red siltstone. Has a very fine-upper to fine-lower grain size and appears well-sorted.
CST-2016-063	38.41575	-110.78446	Soil sample / Unconsolidated	Fenrir (CSA-004) representative sample. Unconsolidated quartz rich sample (collected as powder) on basin floor.	Pinkish-white-red, weakly consolidated sediment. Very fine grain size.

Appendix 2. Calibration of stand-in instruments

This section provides the field calibration procedures for the stand-in instruments performed daily by the on-site field team. Where appropriate, recommendations are also provided for planning and implementation of similar analogue mission scenarios. Calibration procedures were performed on each instrument as per the recommended instructions provided by the instrument manufacturer or the mission control Science Team and/or instrument lead (see Caudill et al., 2019). In 2016, instrument calibration was enhanced by the utilization of four well-characterized standards (CSA-001 to 004) that were collected from the field site during the 2015 CanMars operations; descriptions are provided in Appendix 1. It is recommended that calibration and operational procedures be presented to the Science Team prior to the start of the mission so that all team members understand the capabilities and limitations of the instruments, and sound decisions can be made on their use during daily planning of the mission (see also, Caudill et al., 2019). The following is a detailed explanation of the calibration procedures used for each instrument during the 2016 mission.

Portable-X-Ray Fluorescence Spectrometer: Calibration consisted of running each standard (laboratory-characterized sedimentary sample suite hypothesized to represent field site lithologies) once for 60 seconds and providing the results to the mission control instrument lead as part of the data uplink. The instrument lead could infer the relative accuracy of the rover results by comparing the calibration results with the known values of the standards, which were previously collected by XRF at the University of Western Ontario Biometrics laboratory.

Visible-InfraRed (Vis-IR) Spectrometer: The white balance, dark balance and background scatter values were calibrated using a ceramic white plate. The instrument was calibrated at the outcrop, for approximately 15 seconds, with the optical focus directed at the white plate. If correct, the spectra intensity would flat-line. Data acquisition would then commence, with recalibration at each new outcrop to take into account temporal spectral creep due to subtle variations in the instrument (for example caused by the battery power level) and due to the orientation of the outcrop (e.g., in shadow versus full sunlight). The latter was particularly relevant during phase one of the 2016 CanMars deployment, when the non-contact optical piece, which is more susceptible to variations in light intensity, was operated.

Rockhound DeltaNu Raman Spectrometer: A pure silicon sample was analyzed prior to field data acquisition. The calibration served to estimate the spectra drift correction required, based on the discrepancy between the spectra peak and the expected Si peak of $520 cm^{-1}$. A second calibration was performed using a polystyrene standard, the results of which were compared to an internal library and reported as a correlation coefficient. In the event that a coefficient <0.95 was returned, the spectrometer parameters were adjusted until a coefficient value of 0.95 or greater was achieved.

B&WTek 532 Raman Spectrometer: As with the DeltaNu, a pure silicon sample was analyzed prior to field data acquisition. The calibration served to estimate the spectra drift correction required, based on the discrepancy between the spectra peak and the expected Si peak of $520 cm^{-1}$.

SciAps Z500 Laser-Induced-Breakdown Spectrometer (LIBS): Calibration involved four standards (CSA-001 to 004) that were collected from the field site in the 2015 CanMars season. Calibration consisted of running each standard once. The results were sent to the mission control lead as part of the daily data uplink. The instrument lead could infer the relative accuracy of the rover results by comparing the calibration results with the known values of the standards, which were previously collected by XRF at the University of Western Ontario Biometrics laboratory.

- We present a field geological assessment of the CanMars analogue mission field site.
- Characterization of terrestrial, analogous Mars landing sites is crucial for mission success.
- In-depth field studies allow an understanding of how to address habitability potential.